3D Nonlinear Site Effects at U.S. Strong Motion Stations

Final Technical Report (FTR)

Award G14AP00064

Term: 06/15/2014-11/14/2016

PI: Domniki Asimaki
(Previously at Georgia Tech, now at the California Institute of Technology)

1200 E. California Blvd, MC 104-44, Pasadena CA91125
domniki@caltech.edu; phone: (626) 395-2742

Abstract

Ground surface topography has been repeatedly shown to aggravate the catastrophic consequences of earthquakes during past events. However, while damage maps, numerical and analytical models, and recorded ground motions qualitatively agree on the effects of surface topography on seismic shaking, the model predictions have been systematically underestimating the recorded topographic amplification by up to one order of magnitude or more. This discrepancy has been partially attributed to idealizations (such as 2D geometry, homogeneity, linear elastic material response, and monochromatic or narrowband propagating pulses) that the predictive models frequently employ to approximate the response of more realistic 3D heterogeneous, nonlinear features subjected to broadband, transient ground shaking. In this project, we used high-fidelity numerical simulations to understand how the above idealizations contribute to the systematic underestimation of topography effects, aiming to reduce the quantitative gap between predictions and observations of this phenomenon. The most important finding of this work is that the causative factor of topography effects is not topography alone, but instead is the nonlinear coupling of ground surface geometry and underlying soil stratigraphy which affects the amplitude, frequency, duration and direction of wave propagation. We furthermore show that this coupling is nonlinear --in the sense its effects cannot be captured by superposition of wave propagation through homogeneous topographic features and layered flat media, even if the underlying soil behavior is linear. We expect that our findings will have significant implications on extreme ground motion predictions; on ground motion prediction equations; and on physics-based simulated ground motions and hazard maps, which we should revisit to properly parameterize and simulate 3D site effects by accounting for site, topography and the coupling effects thereof.

Technical Report

1. Introduction

Topography effects are associated with the presence of strong topographic relief (hills, ridges, canyons, cliffs, and slopes), complicated subsurface topography (sedimentary basins, alluvial valleys), and geological lateral discontinuities (e.g., ancient faults, debris zones). These features have been shown to significantly affect the intensity, frequency content and duration of ground shaking during earthquakes. Examples of records attributed in part to topographic amplification are the PGA=1.82g recording of the hilltop Tarzana station during the 1994 Northridge Earthquake [1], the Pacoima Dam (PGA=1.12g) recording during the 1971 San Fernando earthquake [2], the recent extraordinary ground motion (PGA=2.74g) recorded at K-Net station MYG004 during the 2011 Tohoku Earthquake on the crest of a 5m high, steep man-made slope [3], and numerous others (see review studies by [4,5,6]).

Observational evidence from past earthquakes indicates that damage concentration occurs where steep slopes or complicated topography are present; buildings located on the tops of hills, ridges, and canyons, suffer more intense damage than those located at the base. There is also strong-recorded evidence that surface topography affects the amplitude and frequency content of the ground motions. Reviews of such instrumental studies and their comparison to theoretical results can be found in [5-8]. Among others, a case study on the response of a steep site in the Southern Alps revealed a crest-to-base spectral ratio of 20 [9]. In another case study, records obtained on a small ridge revealed that their spectral ratio to recorded motions at a nearby station on flat ground were only a function of topography and site conditions, and were nearly independent of the azimuth, distance, and size of the seismic events [10]. Prompted by observational and instrumented evidence, the problem of scattering and diffraction of seismic waves by 2D idealized topographies on the surface of elastic homogeneous half-spaces has been studied by many researchers [11-19]. A limited number of studies on complex configurations such as topography with soil layering and/or 3D effects can be found in [20-25,42-43].

Geli et al. [6] compiled instrumental evidence and theoretical results on topography effects, and their findings can be summarized as follows: (a) There exists a qualitative agreement between theory and observations on ground motion amplification at ridges and mountaintops and de-amplification at the base of hills; (b) from a quantitative viewpoint, however, there exists clear discrepancy between theory and observations; while there are cases where observations are in good agreement with the numerical results, there also exist numerous cases where the observed amplifications are significantly larger than the theoretical predictions. The most prominent sources of this discrepancy that have been identified are: (i) the focusing of seismic rays in 3D topographic features, which is stronger than the focusing predicted by idealized 2D configurations; (ii) the reverberations and scattering of seismic waves in stratified, heterogeneous soil formations that cannot be simulated using idealized homogeneous media; and (iii) the assumption of linear elasticity, that may not be applicable to describe topography effects for strong shaking associated with nonlinear soil response in the near surface.

There are only a few well-documented case studies demonstrating the severity of topographic effects for strong ground motion. Among them, the PI and coworkers [4,24-25,42] have demonstrated that the substantially higher amplification levels recorded on topographic features (relative to published analytical and numerical predictions) can be in part resolved by accounting for the 3D nature of seismic wave propagation in the near surface of non-flat sites that do not conform to 1D site response conditions. We refer to these effects as 3D *site effects*. Examples include a case study from the M_w5.9 1999 Athens earthquake in Greece, where the observed amplification of seismic motion in the vicinity of a cliff crest could only be predicted by simultaneously accounting for the topographic geometry, stratigraphy and nonlinear site response [24]. One should also

point out the analysis of the Tarzana Hill recordings from the M_w5.9 1987 Whittier Narrows and the M_w6.7 1994 Northridge earthquakes by Graizer [43], who showed that the observed unusual amplification was the combined effect of topography and energy trapped in a low velocity layer at the near-surface. More recent work by the PI and coworkers from the 2010 Haiti and 2011 Tohoku earthquakes [42,57] demonstrated that 3D site effects were the causative factor of observed localized structural damage and recorded exceptionally high ground motion PGA (up to 2.79g at station mygh04).

Topography effects have been accounted for in large-scale ground motion simulations for densely populated seismically active areas in recent years [26-41]. The majority of these studies include the combined effects of seismic source and of highly heterogeneous 3D velocity models with detailed near-surface description of sedimentary deposits below the geotechnical layers; a few of these models also include surface topographic irregularities based on high resolution Digital Elevation Maps. Computational constraints, however, limit the upper bound frequency of these simulations to 2Hz, namely to wavelengths much longer than the thickness of near surface soil formations. Consequently, while the effects of topography are demonstrated for long period waves [40], the effects of smaller features, the coupling between 3D soil and topography effects is not accounted for. On the other hand, broadband ground motion simulations up to 10Hz or more are computationally prohibited from including high impedance soft near-surface velocity materials; in this case, the coupling effects are accounted for through empirical *correction* factors that are based on assumptions of one-dimensional site response and are not properly parameterized to capture the nonlinear physics of soil-topography coupling in wave propagation.

In this study, we investigated the effects of surface topography coupled to the resonance effects of subsurface soil stratigraphy. We started by performing a systematic analysis on the soil-topography coupling effects for parameterized, canonical 2D convex layered features, aiming to understand how the modeling and parametric uncertainty of geometry and material properties of the subsurface layered media compared to the same geometric feature on homogeneous halfspace.

2. Parametric Study of 2D Soil-Topography Coupling (Site) Effects: Canonical cases

In this section, we systematically investigate the soil-topography coupling effects for a 2D dam-type topographic feature. Figure 2.1 shows the configuration of two layered models subjected to vertically propagating *SV* wave. In addition to dimensionless parameters of homogeneous model i.e. $\eta = H/\lambda$ and $\zeta = D/\lambda$, we need to define a set of new parameters accounting for upper layer geometry and material. They consist of dimensionless free-field thickness of upper layer ($\xi = h/\lambda$) and the ratio of shear wave velocities (Q), which is less than unity for near surface soft layer. All the simulations are performed for slope angle $\alpha = 45°$, Poisson's material ($\nu = 0.25$) and unit dimensionless high ($\eta = H/\lambda = 1$). We present the variation of horizontal peak amplification with the dimensionless width for several combinations of Q and ξ. Furthermore, plots of seismogram synthetics, spatial variation of amplification factor and snapshots of wavefield at different time steps are presented for discussion purpose.

Before we go through the results, let us speculate about the response of layered models based on our previous findings for homogeneous dam-type topography. For the layered model with horizontal interface, henceforth denoted by *M1*, we solve a similar problem as in the case of single layer dam (no refraction for vertical incidence). However, there are two differences between *M1* and the original problem. First, we have incoming wave of less energy depending on the stiffness contrast. For stiffness ratios considered in this study, the soil amplification (1D site response) controls the overall behavior at far-field and gives rise to larger amplification factors. Another deviation of *M1* from the original problem is its shallower depth. This results in multiple reflections between two layers (the stiffness contrast controls the number of reflections) and higher order diffracted waves (both body and surface) from tips and toes. The layered model of

parallel interface, referred to as *M2*, has more sources of scattering (tips and toes of interface) and narrower surface region for trapping the incident energy. Therefore, we expect to see a larger number of reflections between two layers compared to model *M1*. Figure 2.2 shows the peak amplification curve as a function of normalized width for both layered models and several sets of Q and ξ. In each curve, the blue curve denotes the response of single layer topography. As we expected, the amplification curves of layered models are similar to that of single layer. The peak amplification factor occurs at the same dimensionless width as in the single layer case ($\zeta = 0.88$). Furthermore, they are clustered in three different categories (black, red and blue) based on the stiffness contrast with higher values at larger contrast. The dimensionless thickness of upper layer, on the other hand, has little effect on the amplification response. This is also expected as the constructive interference of first arrivals (direct and diffracted waves) gives rise to peak amplification. The lower plot of Figure 2.2 shows a different wave mechanism for model *M2*. First, they are no longer similar to the single layer model inasmuch as peaks and troughs occur at different dimensionless widths. In addition, there is no clustering based on stiffness contrast. Instead, the thickness of upper layer play a more important role in the form of amplification curves. One could see that curves of the same line type and different colors are almost similar. This is because the free surface boundary and interface form a single scatterer whose characteristic length (thickness) controls the consequent wavefield. Finally, the threshold dimensionless width, beyond that the dam response turns into that of single slope, is much larger than model *M1*. For example, the amplification curve of $Q = 4$ and $\xi = 1/4$ is still changing at $\zeta =$ 4.0. The energy trapped in the upper layer, which reflects back and forth between two boundaries, accounts for such oscillatory behavior.

To complete the discussion, we pick several characteristic points from the amplification curves of each layered model and present more details about the consequent wavefield. Figures 2.3 and 2.4 show the component of seismogram synthetics at the peaks of model *M1* ($\zeta = 0.88$, $\xi =$ 1/4) respectively for stiffness contrast 2 and 4. They have the same general structure (diffracted surface and body waves from tips and toes on both sides) as that of single layer case. A distinguishing feature, which is more pronounced in larger contrast (Figure 2.4), is the reverberation of incoming wave in the upper layer. Traces of low amplitude diffracted Rayleigh waves are masked by those of body waves. Figure 2.5 compares the spatial variation of amplification factor of these layered models with that of single layer. We could check the nonlinear coupling between soil and topography amplifications in this figure. The blue curve shows the pure topography amplification factor of 2.05. Red and black curves show soil amplification (free-field response) of 1.49 and 2.03 for $Q = 2$ and 4, respectively. We can also extract the total (coupled) amplification factors from these curves as 2.83 and 3.38. It is evident that we cannot obtain the total amplification by multiplying topography and soil amplification factors. We can draw the same conclusion from the vertical component. Figures 2.6 and 2.7 show the snapshots of total wavefield for model *M1* with $Q = 2$ and 4. The middle plots, which correspond to the time of maximum amplification, show the constructive interferences of direct and diffracted wavefields (first arrivals). The third plots show the part of incident energy that is trapped in the upper layer and generates the subsequent multiple reflections. Figures 2.8 to 2.12 and 2.13 to 2.17 show the same set of plots for model *M2* ($\xi = 1/4$ and $Q = 2,4$) at two characteristic width. The first set correspond to $\zeta = 0.88$, where both single layer and *M1* models have a peak amplification. It shows that model *M2* has a trough rather than a peak due to destructive interference at this width. At larger width ($\zeta = 1.84$), however, diffracted surface waves constructively interfere with the transmitted part of incoming wave to form the peak horizontal amplification. This is clearly shown in the middle plots of total wavefield snapshots (Figures 2.16 and 2.17). Comparing the results of model *M2* with those of *M1*, we could interpret the following features:

i. Larger number of multiple reflections because of shallower depth in the middle region (between two toes) and more points of scattering;
ii. Faster attenuation of the scattered wavefield due to more energy leakage within the middle region;
iii. More regular structure of scattered wavefield since the upper layer acts as a unit;
iv. More complex coupling between soil and topography amplifications and hence clearer evidence of its nonlinearity in the middle region (Figure 2.10↑);
v. Having a bi-material medium of irregular interface, both types of surface waves i.e. Rayleigh and Stoneley exist in model *M2*.

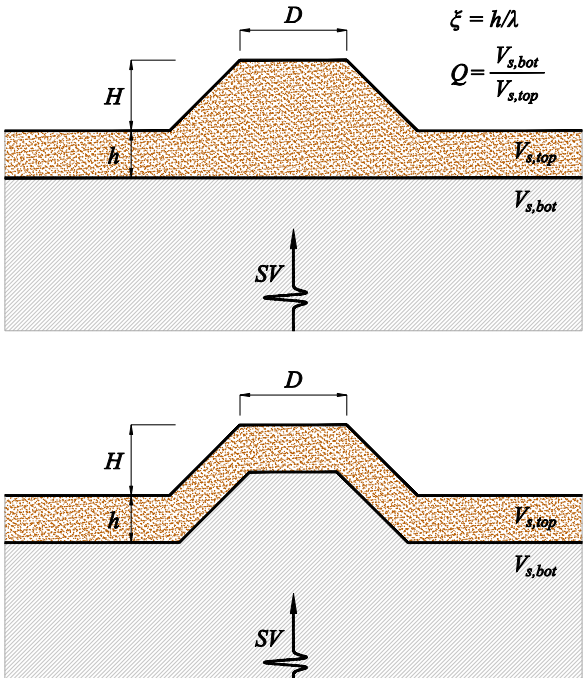

Figure 2.1. Configurations of layered models used for the coupling effect – (↑: *M1*, ↓: *M2*)

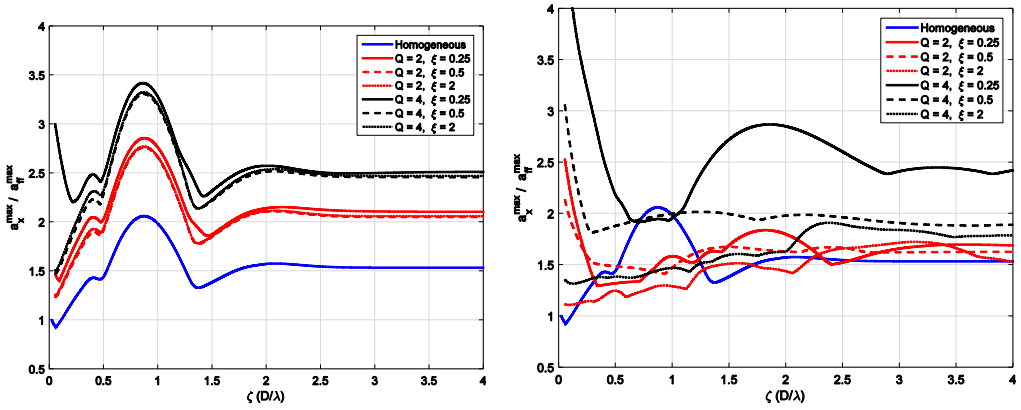

Figure 2.2. Horizontal amplification factor vs. normalized width – (left: *M1*, right: *M2*)

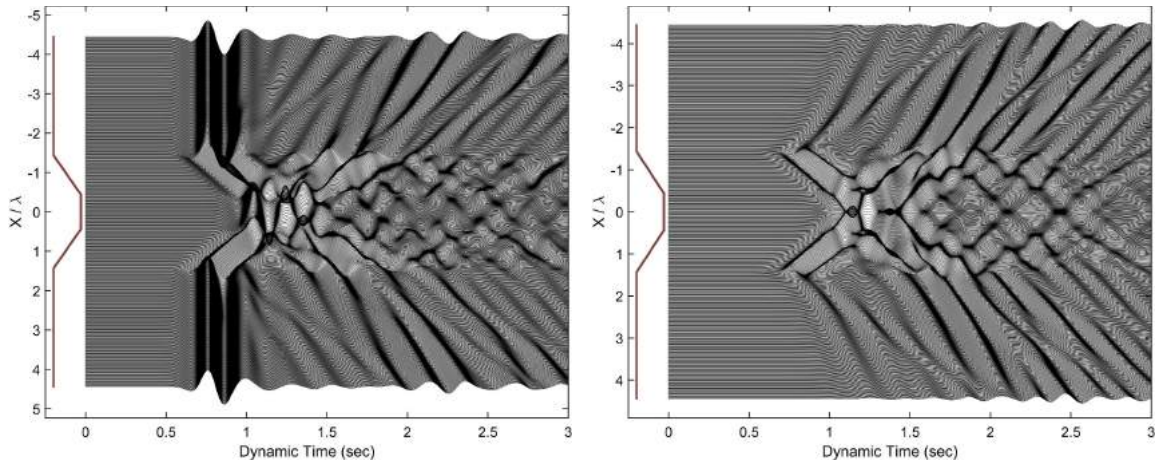

Figure 2.3. Seismogram synthetics of acceleration, M1 (left: H, right: V) – $\zeta = 0.88$, $\xi = 1/4$, $Q = 2$

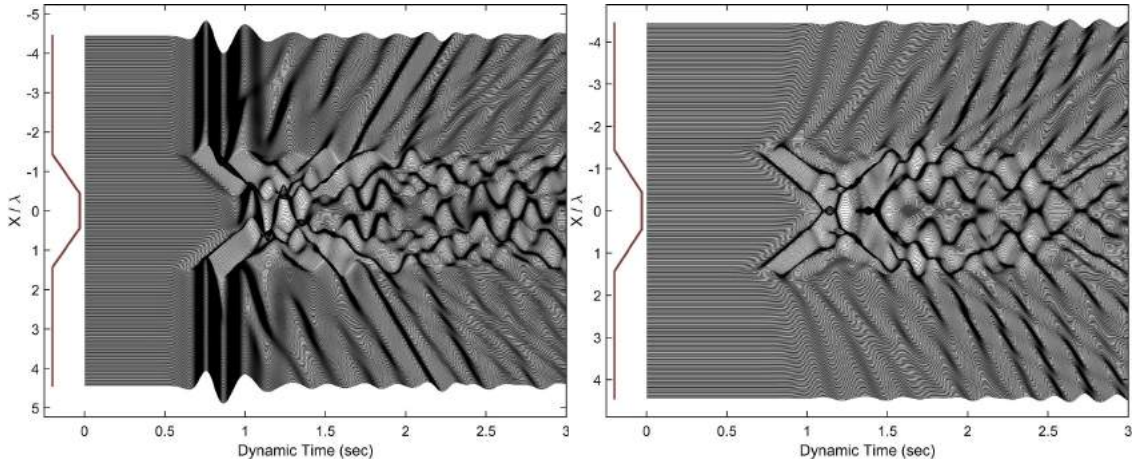

Figure 2.4. Seismogram synthetics of acceleration, M1 (left: H, right: V) – $\zeta = 0.88$, $\xi = 1/4$, $Q = 4$

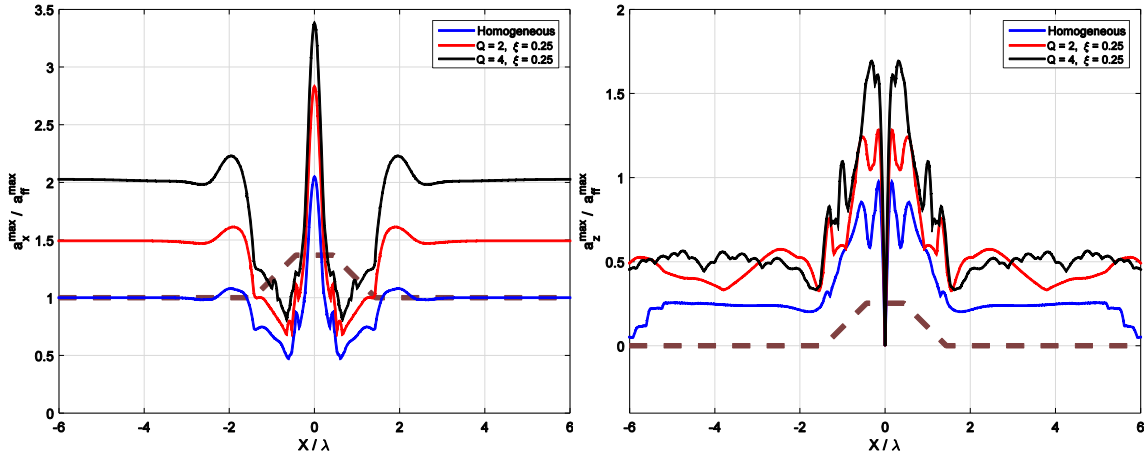

Figure 2.5. Spatial variation of amplification factor for M1 (left: H, right: V) – $\zeta = 0.88$

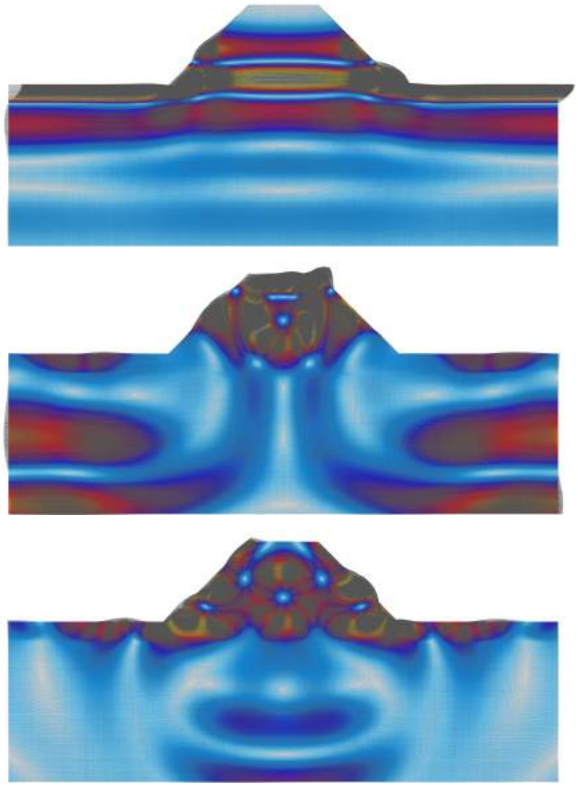

Figure 2.6. Snapshots of total wavefield ($\uparrow$: 0.7s, $\leftrightarrow$: 0.98s, $\downarrow$: 1.5s) – $\zeta = 0.88$, $\xi = 0.25$, $Q = 2$

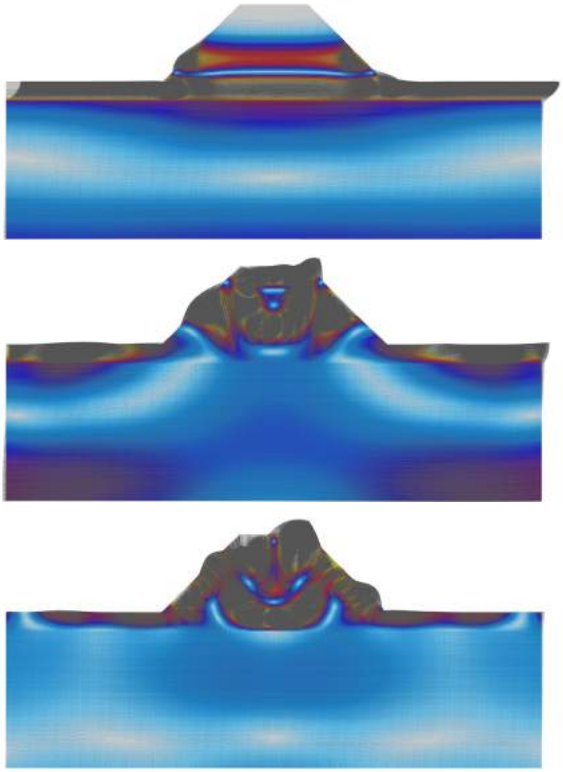

Figure 2.7. Snapshots of total wavefield ($\uparrow$: 0.5s, $\leftrightarrow$: 0.85s, $\downarrow$: 1.2s) – $\zeta = 0.88$, $\xi = 0.25$, $Q = 4$

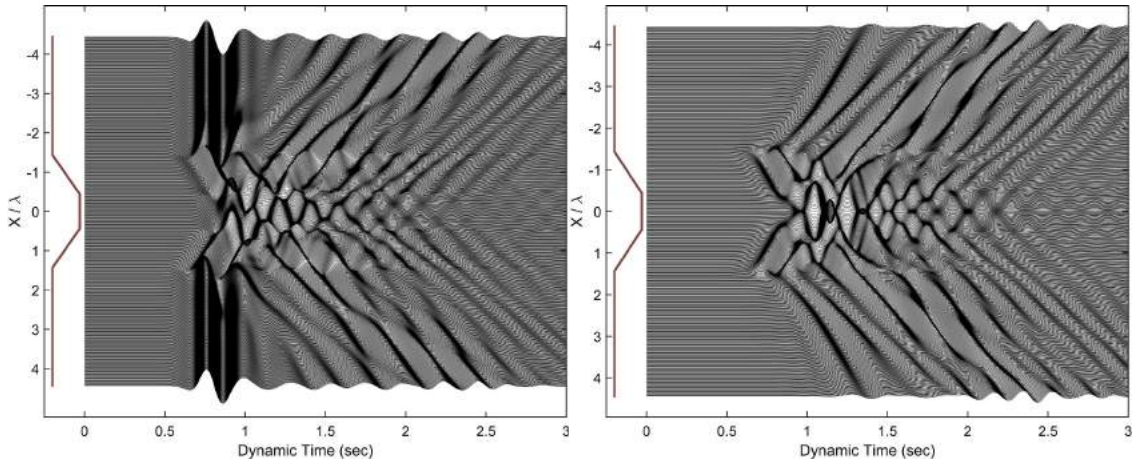

Figure 2.8. Seismogram synthetics of acceleration, M2 (left: H, right: V) – $\zeta = 0.88$, $\xi = 1/4$, $Q = 2$

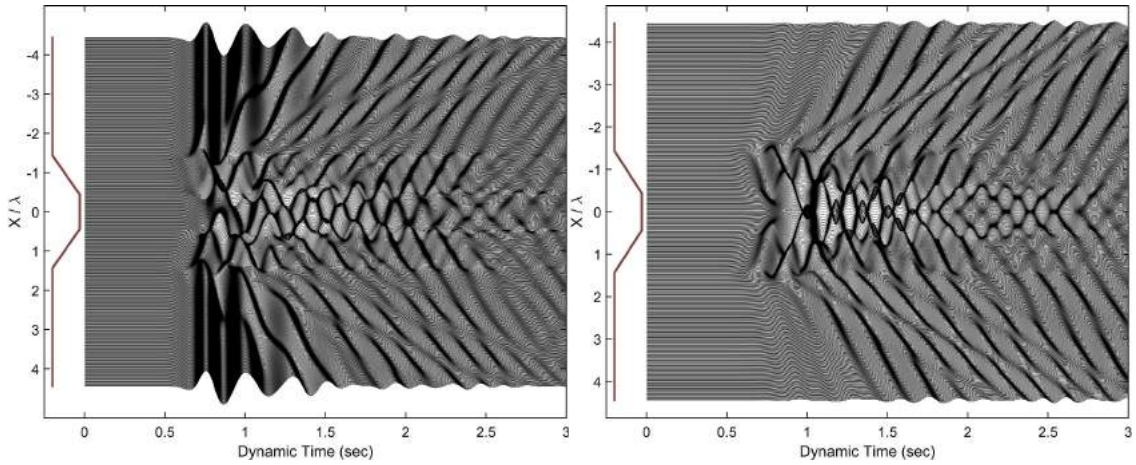

Figure 2.9. Seismogram synthetics of acceleration, M2 (left: H, right: V) – $\zeta = 0.88$, $\xi = 1/4$, $Q = 4$

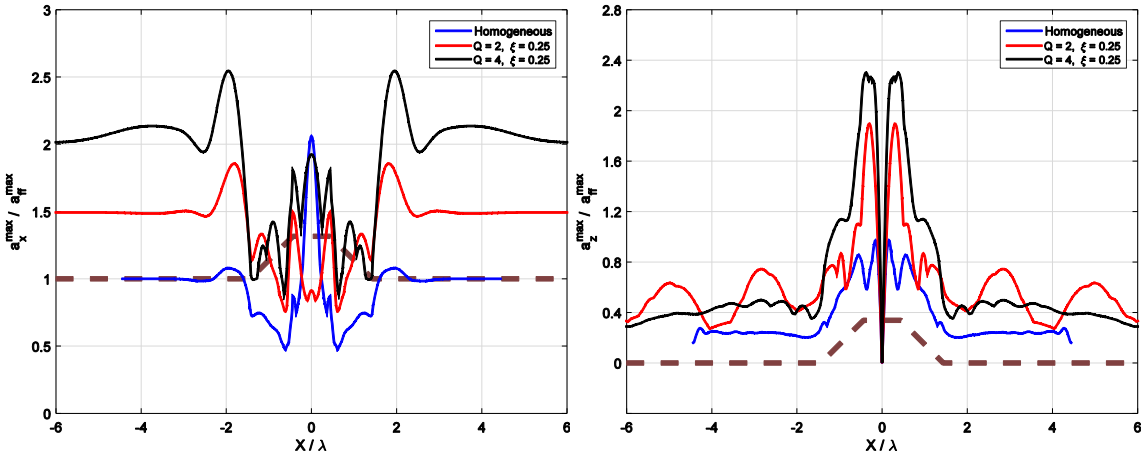

Figure 2.10. Spatial variation of amplification factor for M2 (left: H, right: V) – $\zeta = 0.88$

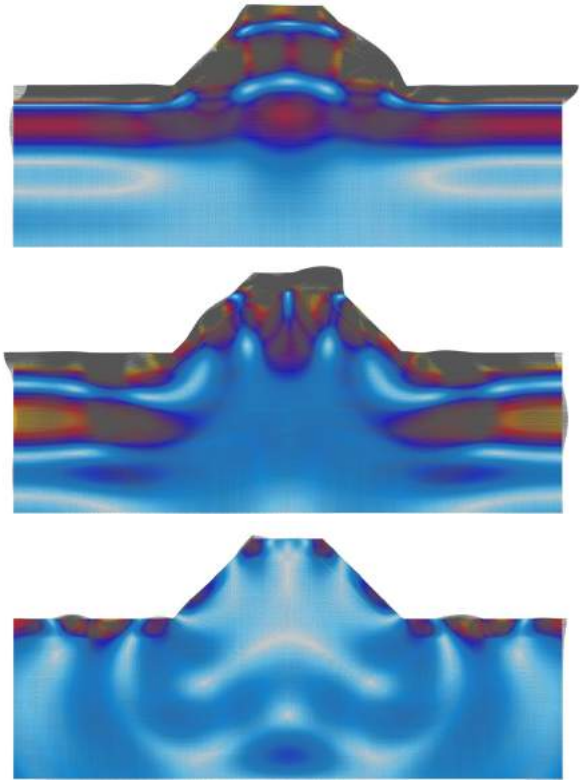

Figure 2.11. Snapshots of total wavefield (↑: 0.7s, ↔: 0.85s, ↓: 1.5s) – $\zeta = 0.88$, $\xi = 0.25$, $Q = 2$

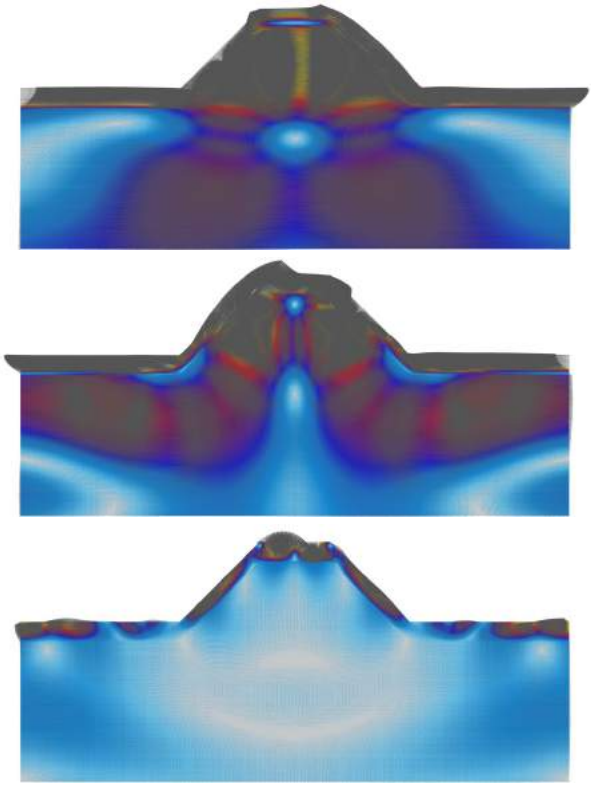

Figure 2.12. Snapshots of total wavefield (↑: 0.5s, ↔: 0.72s, ↓: 1.2s) – $\zeta = 0.88$, $\xi = 0.25$, $Q = 4$

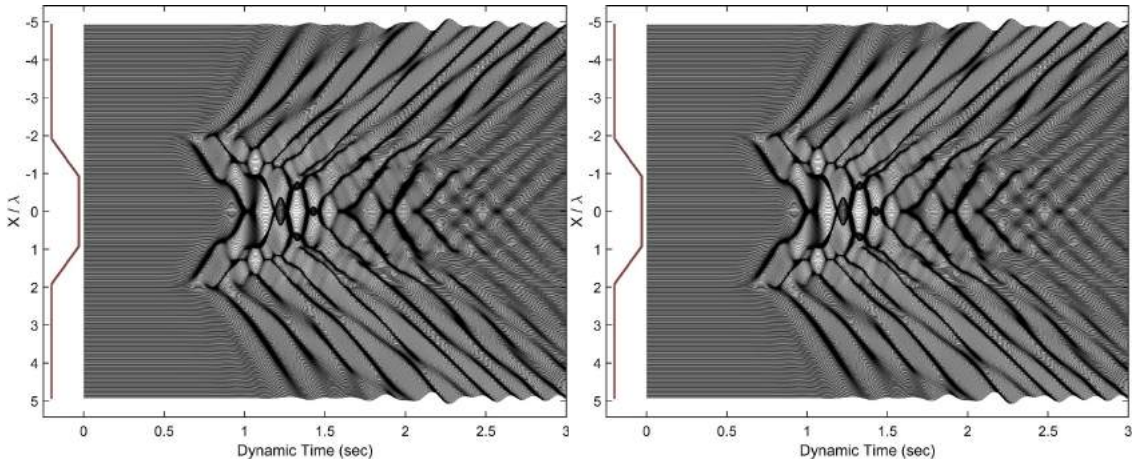

Figure 2.13. Seismogram synthetics of acceleration, M2 (left: H, right: V) – $\zeta = 1.84$, $\xi = 1/4$, $Q = 2$

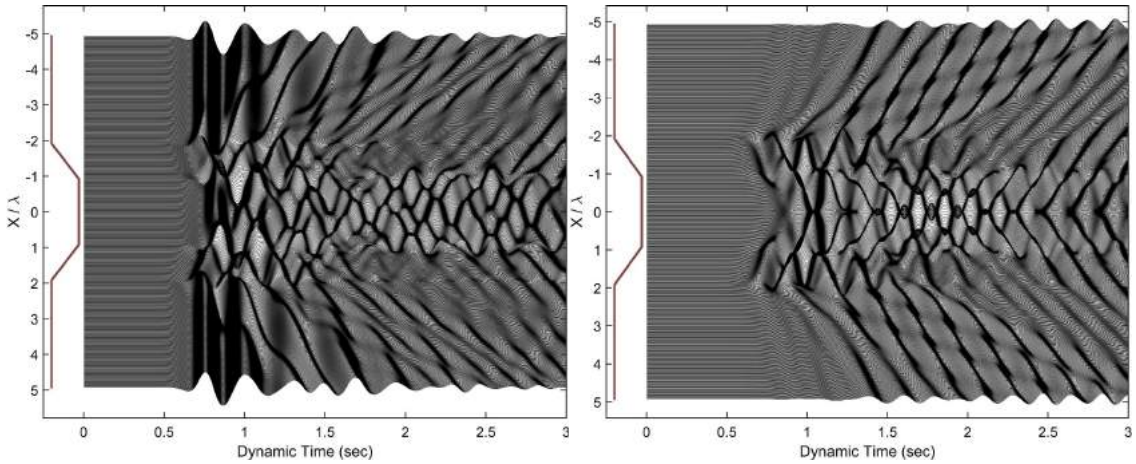

Figure 2.14. Seismogram synthetics of acceleration, M2 (left: H, right: V) – $\zeta = 1.84$, $\xi = 1/4$, $Q = 4$

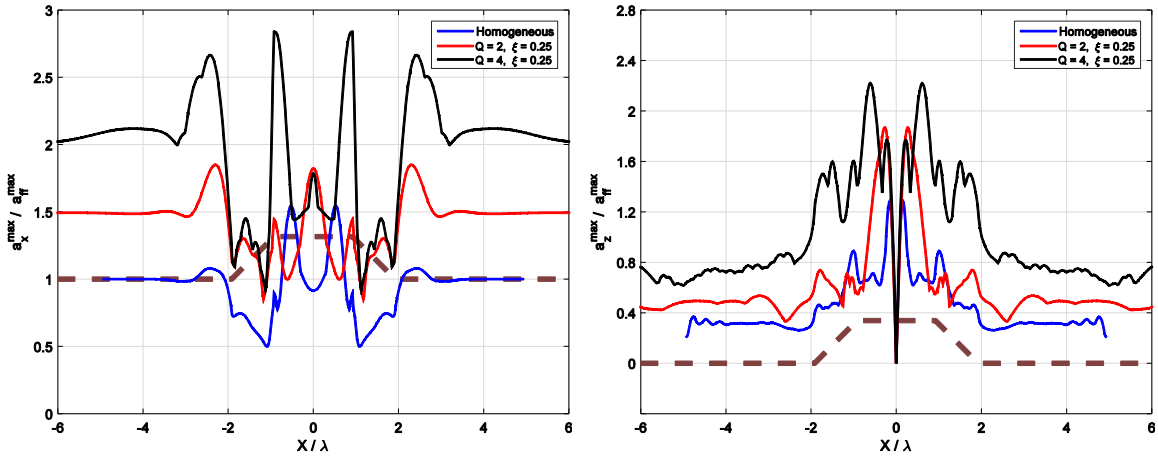

Figure 2.15. Spatial variation of amplification factor for M2 (↑: H, ↓: V) – $\zeta = 1.84$

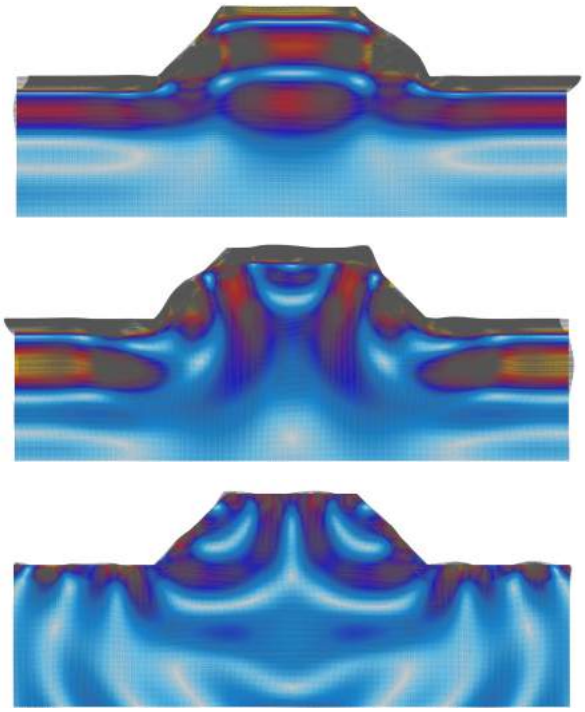

Figure 2.16. Snapshots of total wavefield ($\uparrow$: 0.7s, $\leftrightarrow$: 0.84s, $\downarrow$: 1.5s) – $\zeta = 1.84$, $\xi = 0.25$, $Q = 2$

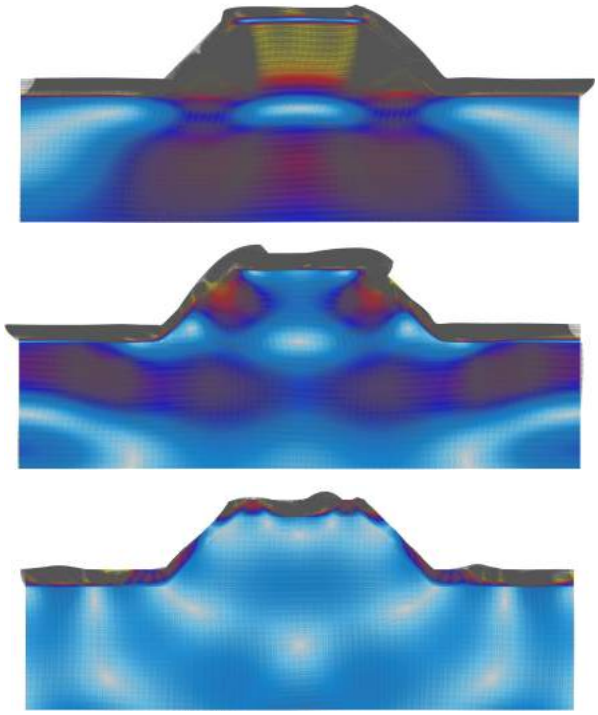

Figure 2.17. Snapshots of total wavefield ($\uparrow$: 0.5s, $\leftrightarrow$: 0.67s, $\downarrow$: 1.2s) – $\zeta = 1.84$, $\xi = 0.25$, $Q = 4$

3. Case Studies

In this section, we investigate the coupling effects of surface topography and soil layering for two actual sites. The first one is BK-KCC strong motion station that represents a "rock site" with a thin weathered crust of softer material. Another case study i.e. CI-LCP station, which is located in southern California, represents a "soil site" with thicker soft layers near the surface. We used DEM data of 1/3 arc-second resolution to construct the 3D surface of topographic map. The region of study, which is an isolated topography or a set of features, has been extracted from the topography surface. To build a model in Cartesian coordinates system, the resulting patch has been later extended to the boundaries of a rectangular region. As for layered models i.e. V_{S30} and true layering, we assumed each near surface layer has a constant depth. In the absence of more detailed geotechnical site investigation, this assumption seems reasonable especially for weathered rock site. Assuming the elastic linear material, properties of different layers have been extracted from the USGS report 2013-1102.

3.1 Strong Motion Station BK-KCC

The bird-eye view of BK-KCC site map is shown in Figure 3.1 along with its topographic map. The location of strong motion station is designated by a yellow triangle on the site map. Figure 3.2 shows the finite difference model used for simulating wave propagation in homogeneous and layered cases (all simulations have been performed using the finite difference code FLAC3D^{TM}). The material properties of different layers are listed in Table 3.1 for each model. The thin crust of weathered rock only presents in the true layering model. We expect to see the effect of this low velocity thin layer in the high frequency range when the short wavelength direct and scattered waves are caught. Two types of excitations have been applied at the base of each model: A single Ricker wavelet of central frequency f_0 = 3.5 Hz and an ensemble of three Ricker wavelets with central frequencies f_0 = 1, 3 and 7 Hz that are superposed at their center. The time histories of these pulses along with their Fourier spectra have been shown in Figures 3.3 and 3.4. It is clearly seen in the topographic map that the feature is not symmetric with respect to the azimuth angle. Therefore, we defined two major axes (based on the geometry and expected wave focusing) along them the input shear wave is polarized (Figure 3.5).

Figures 3.6 to 3.8 show the amplification factor maps overlaid by topography contour lines of 5m interval respectively for homogeneous, V_{S30} and true layering cases. The amplification factor is defined as the ratio of peak ground acceleration of each point to corresponding value of homogeneous model at free-field (FF). Values of peak and free-field amplification factors are also shown on each plot for reference. However, a more important factor in seismic response evaluation is the region of influence. Gridlines help us to have an approximate extension of amplified regions. For the homogeneous model, as it is expected from the geometry, *X*-polarization results in larger amplification. In addition, the pattern is consistent with the general perception of topographic amplification i.e. amplification/de-amplification in convex/concave regions. The isolated model (Figure 3.2) can be considered as a superposition of two topographic features. In fact, the central 3D irregular hill is located on top of the 1D single slope. For each polarization scenario, the amplification pattern of homogeneous model can be explained by the resultant effect of these features. For example, when the incoming shear wave is polarized in the *X* direction, the central feature shows amplification around the top and de-amplification along the toe. The background single slope, on the other hand, is subjected to a SH wave and shows a small amplification in regions *A* and *B*. We can also see amplification in region *C* where there is a 2D dam-type topography subjected to incoming *SV* wave. For *Y*-polarization case, we can see a similar amplification and de-amplification patterns around the central feature. However, the background single slopes plays a more important role as the incoming *SV* wave is amplified behind its crest (regions *D* and *E*). Adding a 30m surface layer of half shear velocity results in

larger amplification over a wider range (Figure 3.7). However, the general amplification pattern and regions are similar to the homogeneous case (pure topography). That is the geometry (thickness) and material properties (stiffness contrast) of upper layer cannot adequately scatter the incoming wave of specified wavelength. Furthermore, while the 1D site response shows 21% increase (1.21) with respect to the homogeneous case, the 3D amplification is only magnified 12% (2.30). This is the first notion of nonlinear coupling between topography and soil layering. Finally, the amplification factors of true layering model have been shown in Figure 3.8 for both polarization. We can see a similar pattern as in the previous cases with a little less amplification with respect to V_{S30} model. Therefore, the V_{S30} model presents an overestimated amplification factors for this site.

In order to understand the energy distribution among various frequency components more clearly, it is useful to obtain the frequency response of topographic feature. Figure 3.9 shows the amplitude of 1D transfer function (surface to borehole) of site BK-KCC. The characteristic behavior of rock sites at low frequencies is clearly depicted in this figure. The fundamental frequency of the site i.e. f_0 = 21.4 Hz is beyond the practical frequency range of interest for Earthquake Engineering (1-15 Hz). The frequency range covered by Ricker ensemble is also highlighted in this figure. Figures 3.10 to 3.14 show the same transfer function values at various frequencies. Over the frequency range of interest, "3D transfer function" has more variations compared to the 1D case. In addition, at lower frequencies, the large wavelength of incoming wave is barely seen by the feature and results in a coarser scattering pattern. Increasing the frequency will result in finer scattering pattern as the incoming energy is captured by features of smaller size.

Figure 3.15 shows snapshots of the total wavefield at different time steps. The top plot depicts amplification of incoming shear wave by the 2D topographic feature (region C in Figure 3.6). The middle one corresponds to the moment of peak amplification when we have maximum constructive interference between incoming shear and diffracted surface waves. The last plots shows that after the direct wave reflected back to the medium, a minor portion of energy remains in the upper layer while the major part is discharged.

Table 3.1. Thickness and material properties for different layering scenarios – site BK-KCC

Layering Scenario	Layer	Thickness (m)	V_S (m/s)	ν	ϱ (kg/m^3)
Homogeneous	1	---	2445	0.3	2500
V_{S30}	1	30	1252	0.3	2390
	2	---	2445	0.3	2500
True Layering	1	2.5	239	0.3	1870
	2	6.0	1072	0.3	2300
	3	6.0	1865	0.3	2400
	4	---	2445	0.3	2500

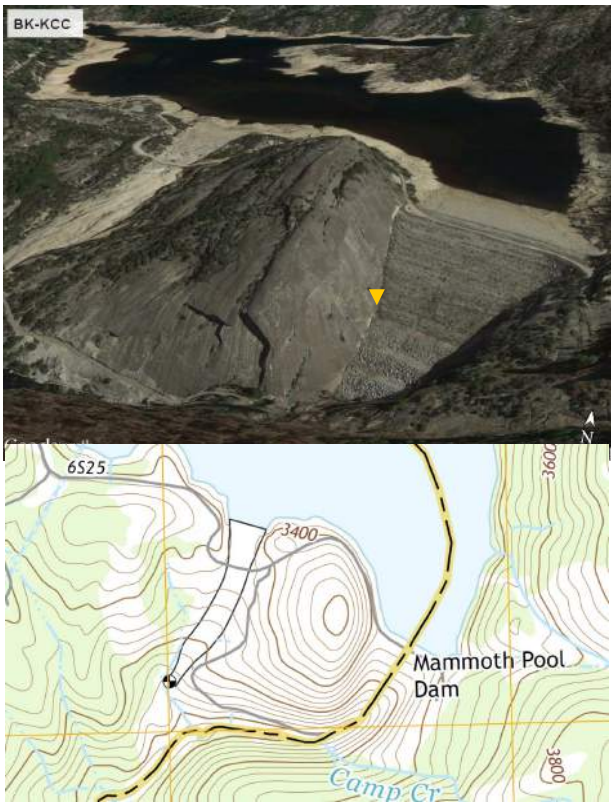

Figure 3.1. BK-KCC site – ↑: bird-eye view, ↓: topographic map

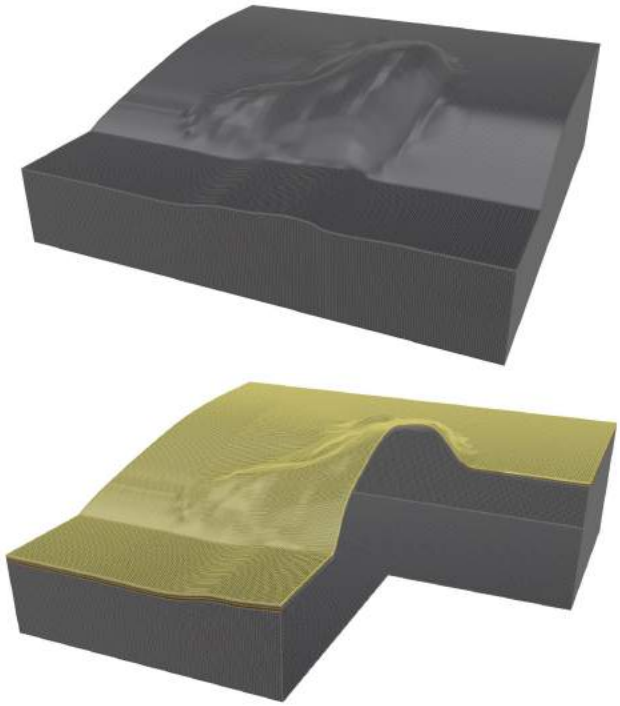

Figure 3.2. Numerical model used for BK-KCC station – ↑: homogeneous, ↓: true layered

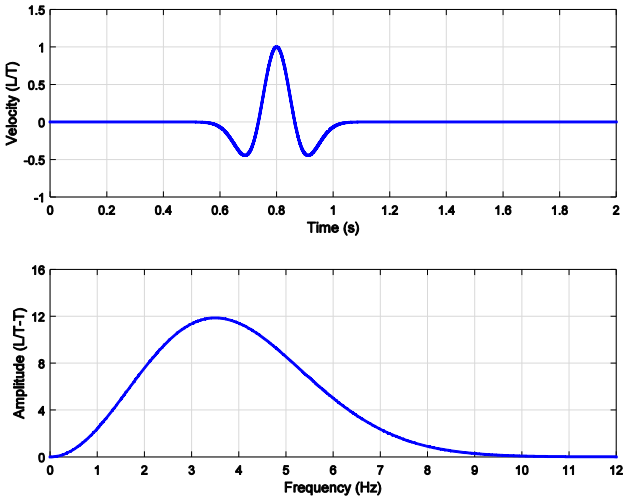

Figure 3.3. Ricker wavelet and its Fourier Spectrum

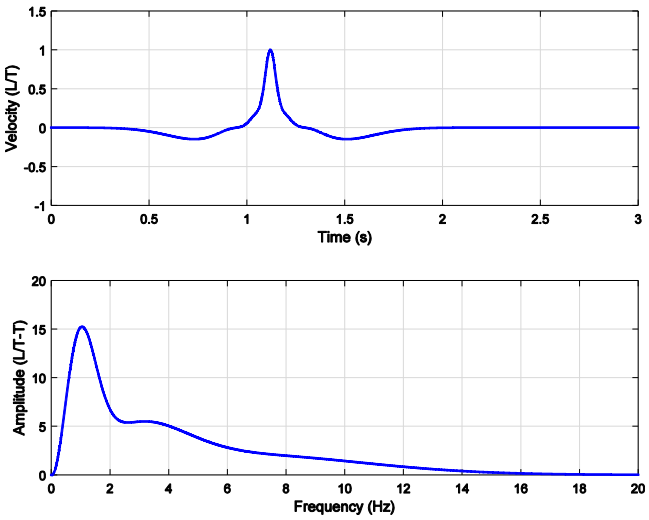

Figure 3.4. Ricker ensemble and its Fourier Spectrum

Figure 3.5. Polarization directions of input shear wave – site BK-KCC

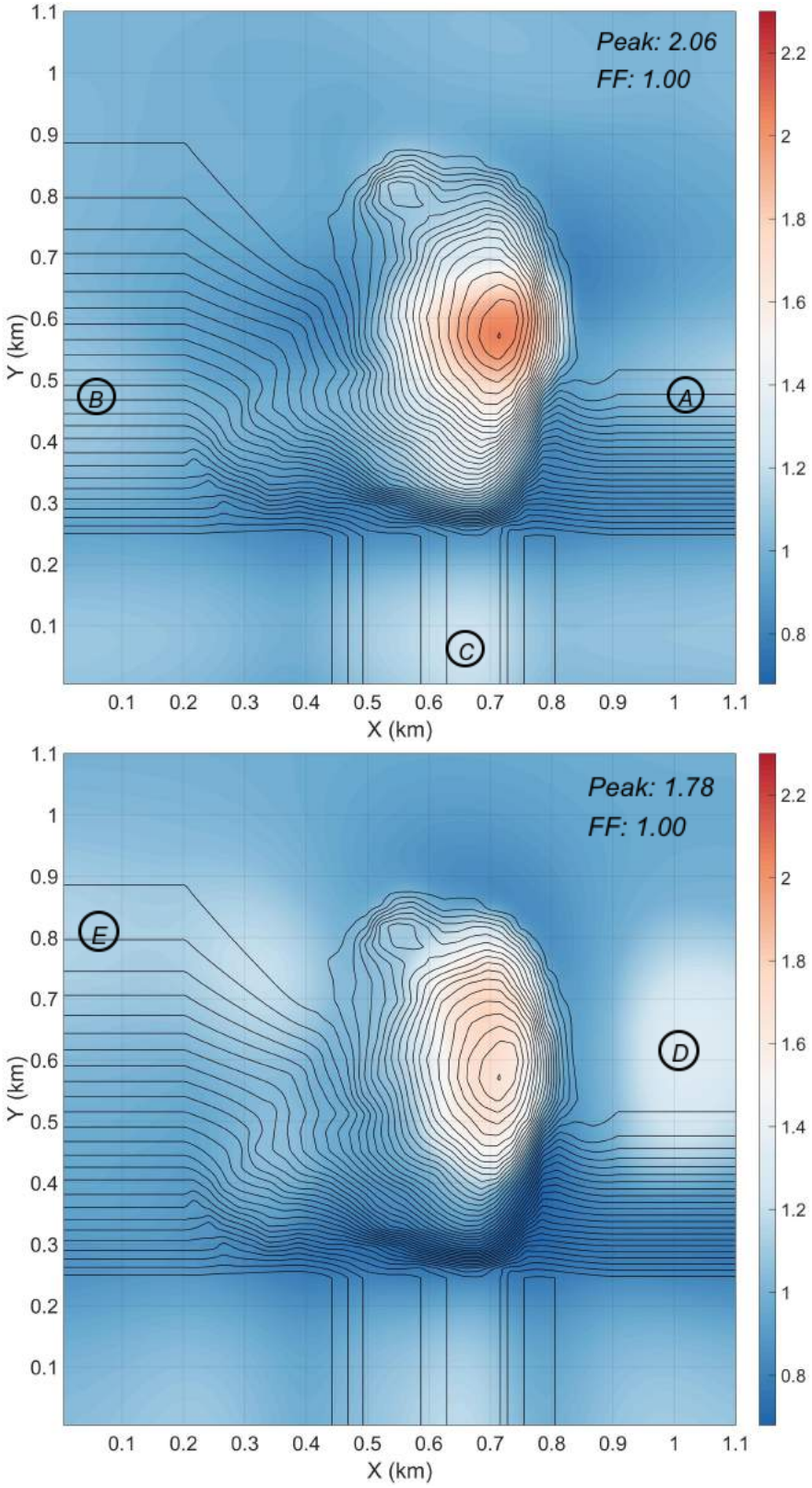

Figure 3.6. Amplification factor for homogeneous case, BK-KCC – ↑: X, ↓: Y polarization

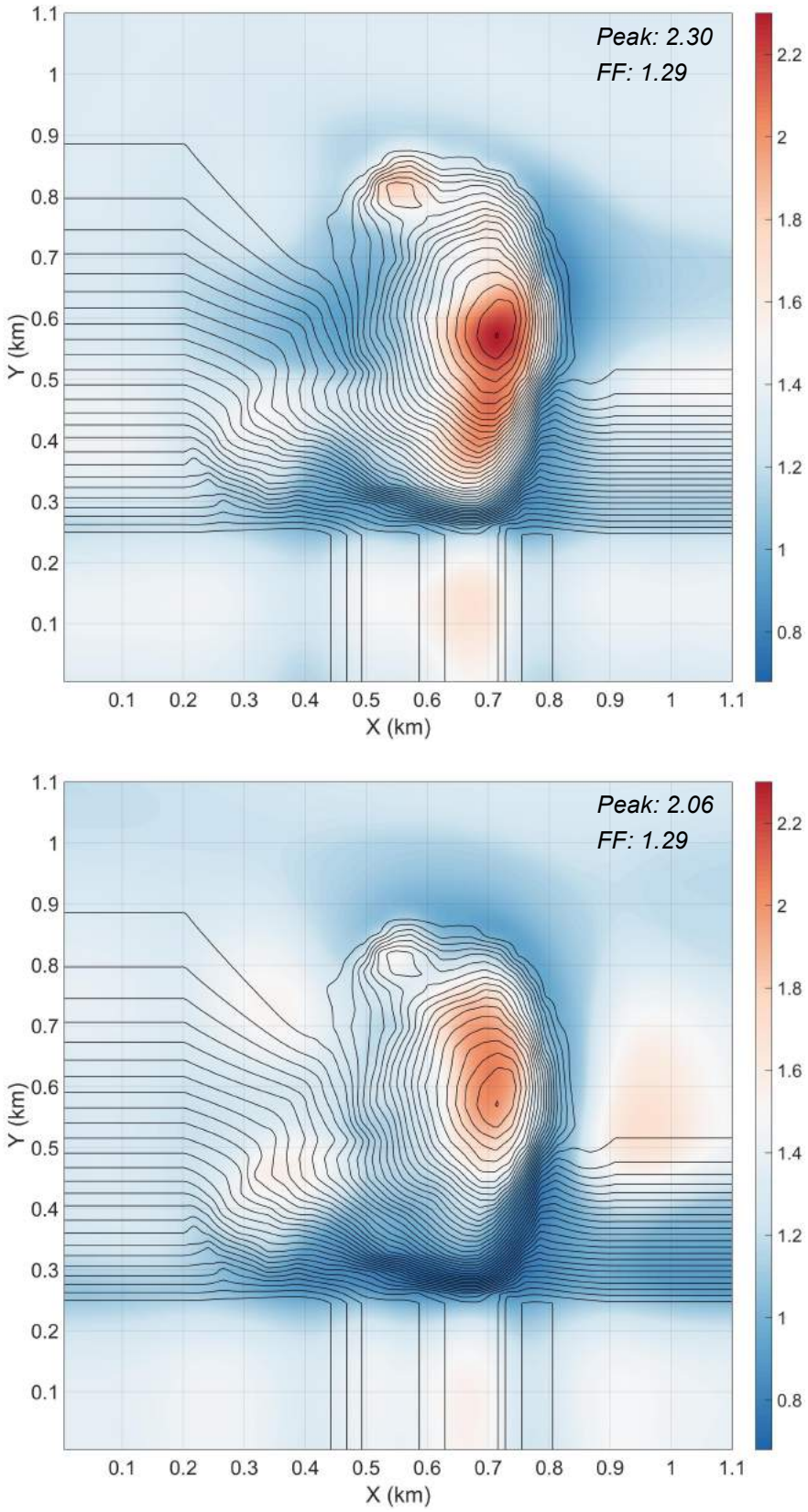

Figure 3.7. Amplification factor for V_{S30} case, BK-KCC – ↑: X, ↓: Y polarization

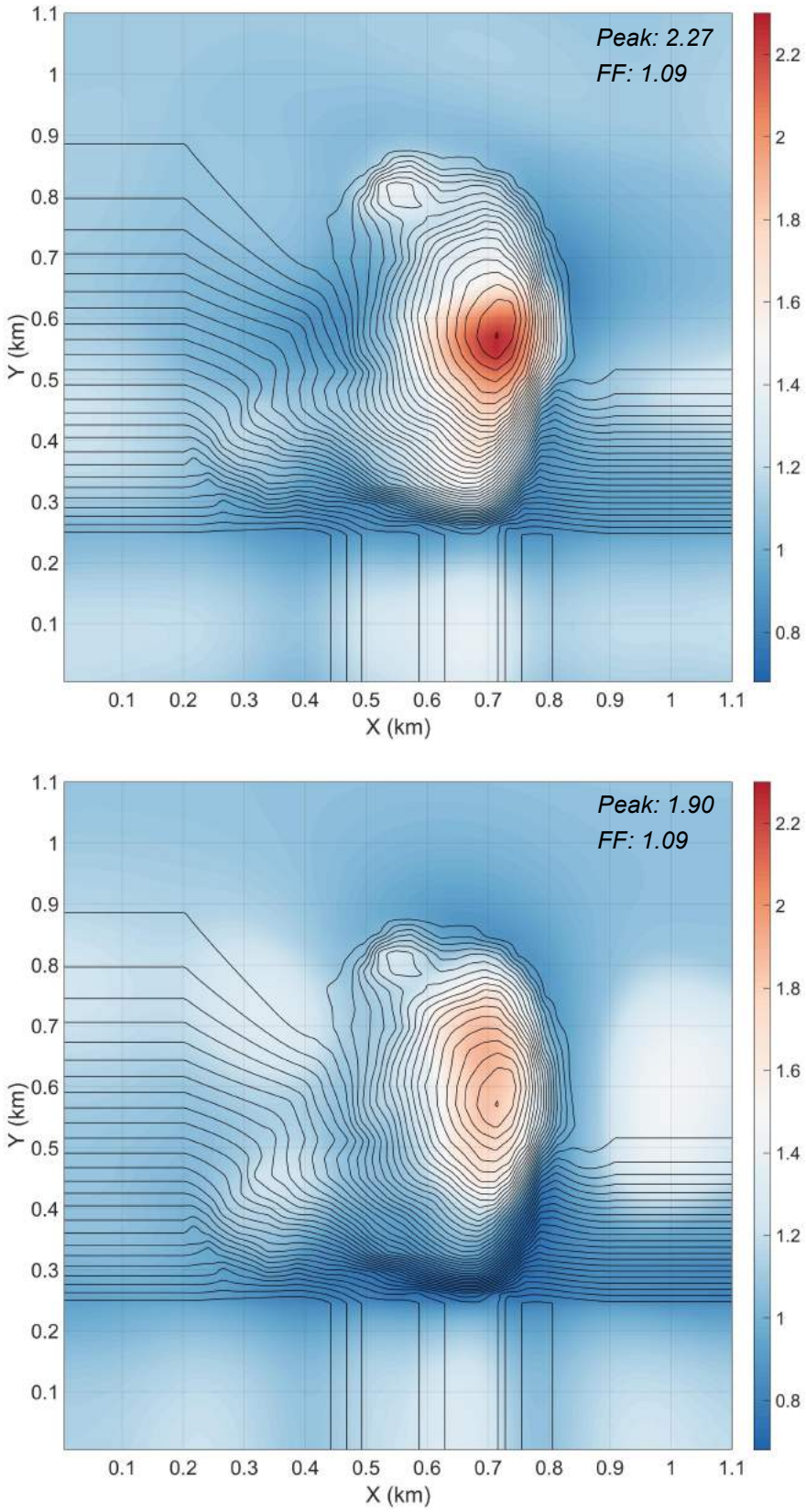

Figure 3.8. Amplification factor for true layering case, BK-KCC – ↑: X, ↓: Y polarization

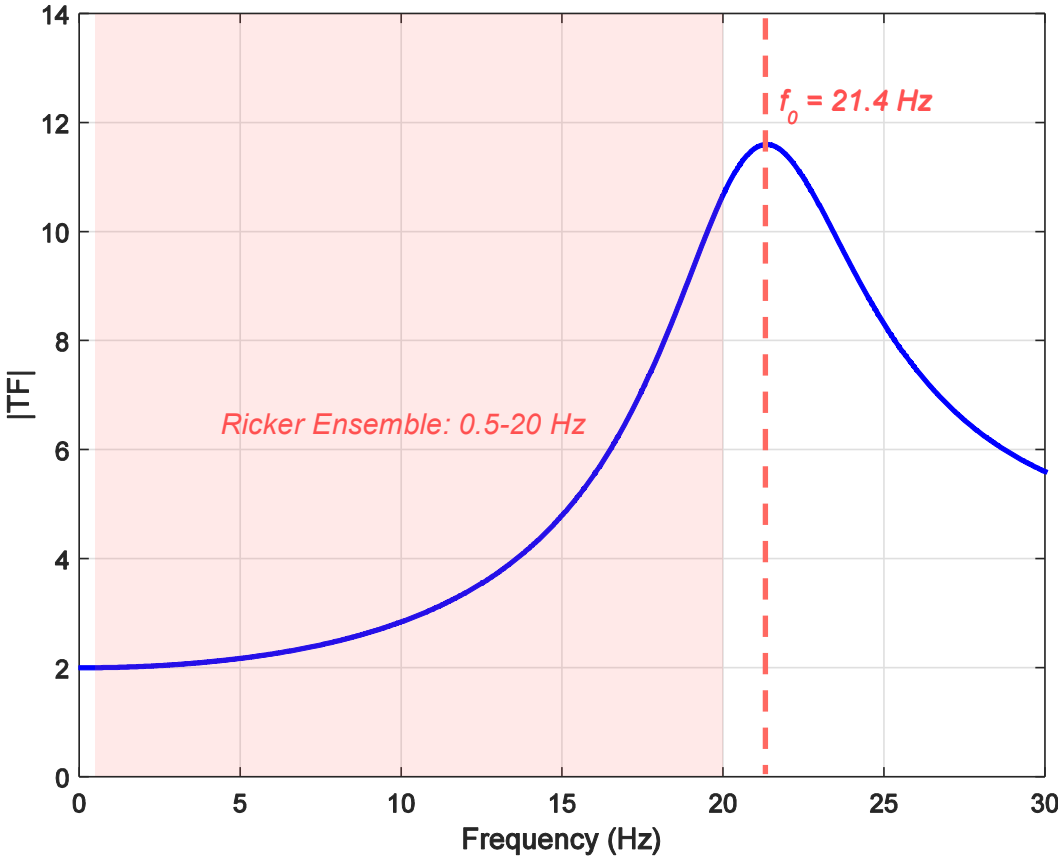

Figure 3.9. 1D transfer function for site BK-KCC

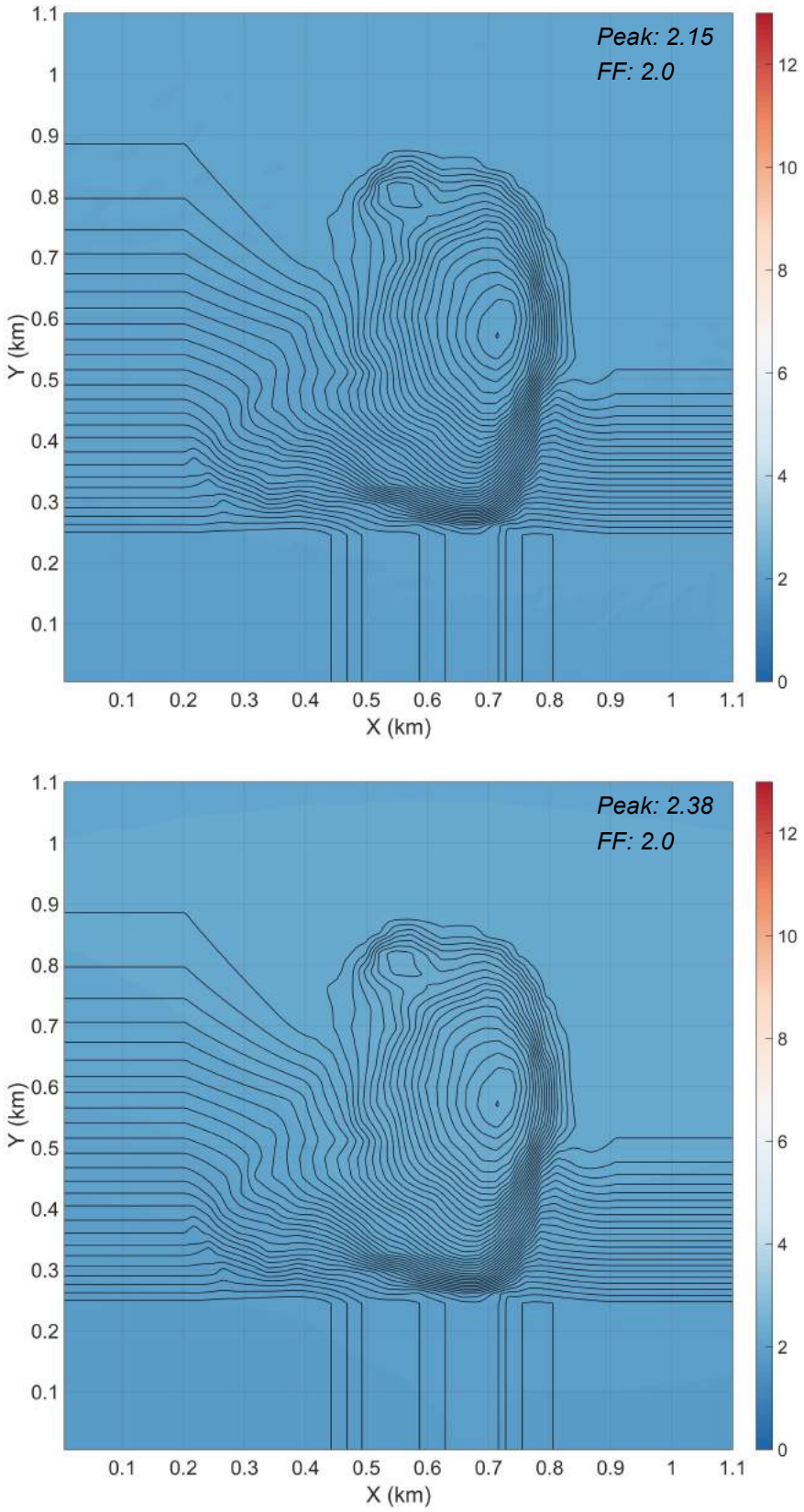

Figure 3.10. Transfer function amplitude of true layering, BK-KCC – ↑: $f = 0.5$ Hz, ↓: $f = 1$ Hz

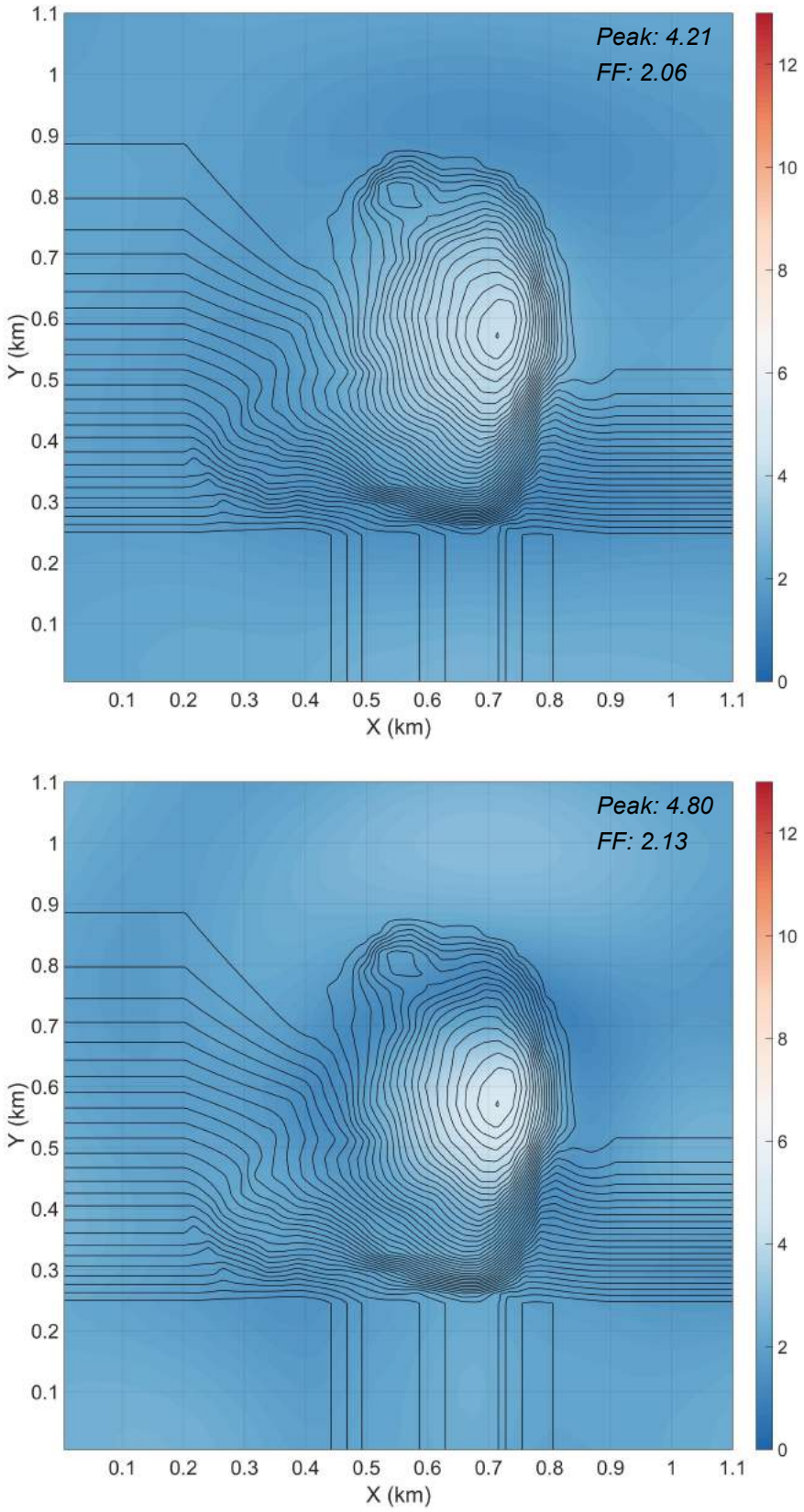

Figure 3.11. Transfer function amplitude of true layering, BK-KCC – ↑: $f = 3$ Hz, ↓: $f = 4.5$ Hz

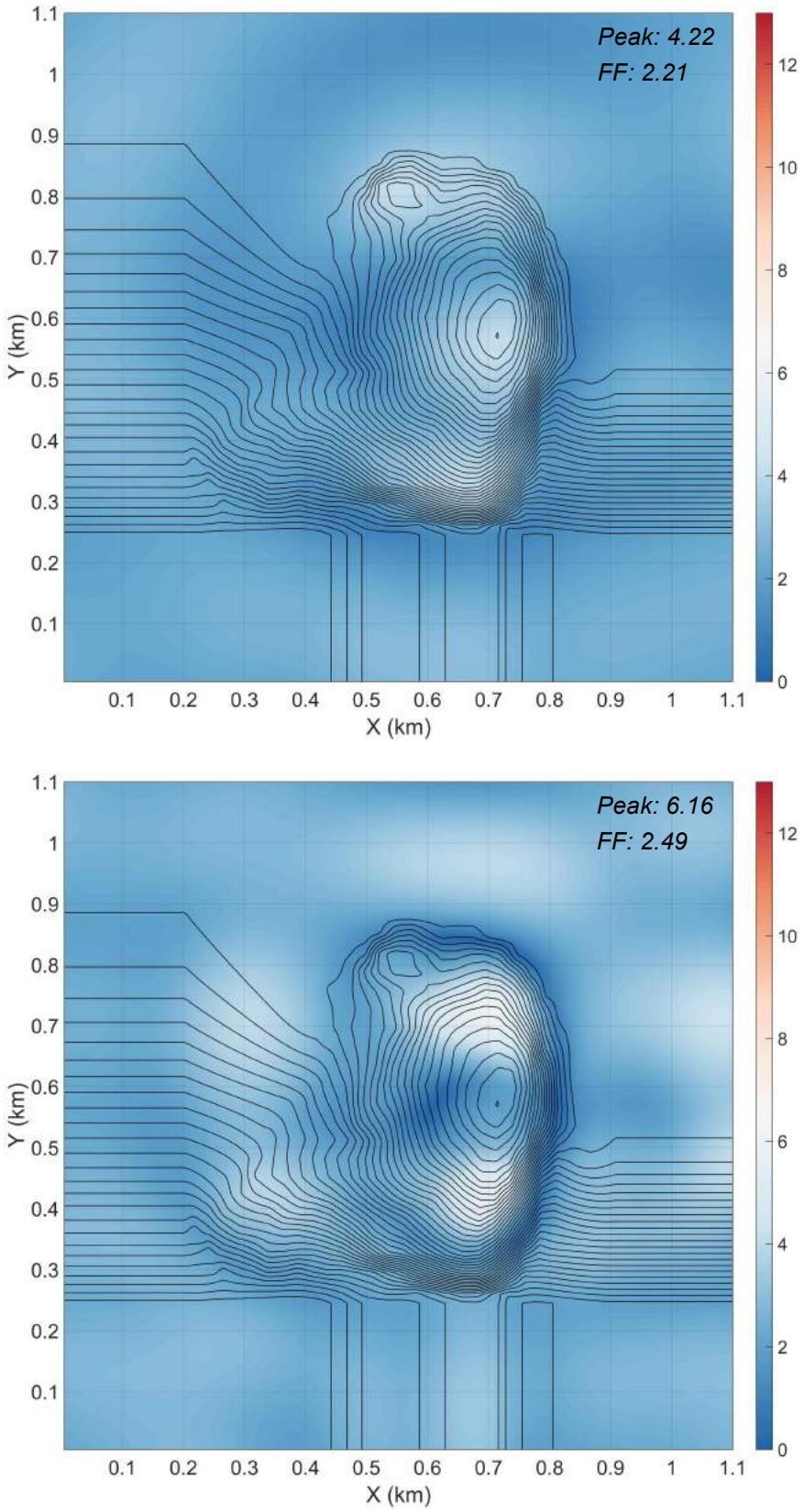

Figure 3.12. Transfer function amplitude of true layering, BK-KCC – ↑: $f = 5.5$ Hz, ↓: $f = 8$ Hz

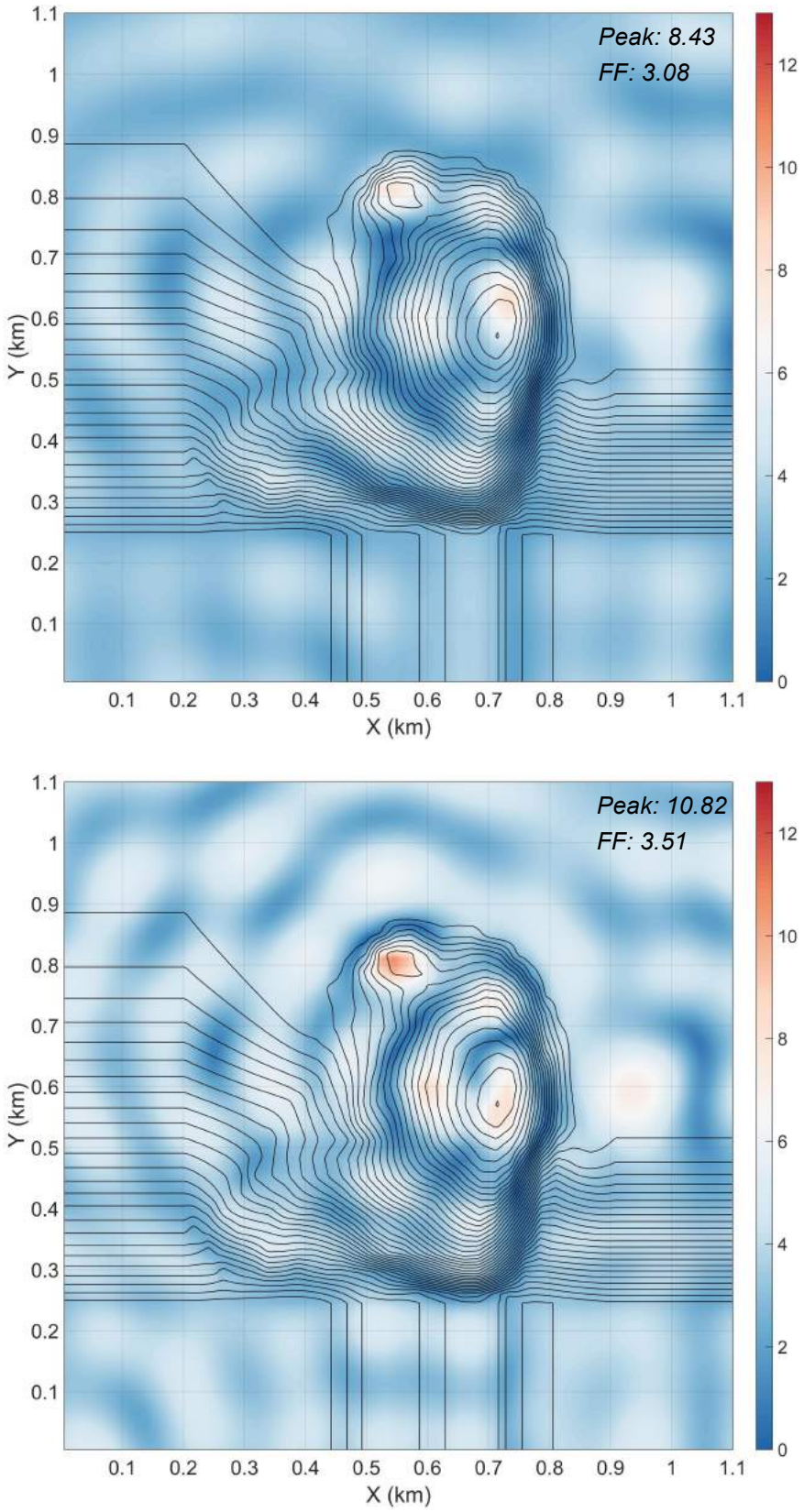

Figure 3.13. Transfer function amplitude of true layering, BK-KCC – ↑: $f = 11$ Hz, ↓: $f = 12$ Hz

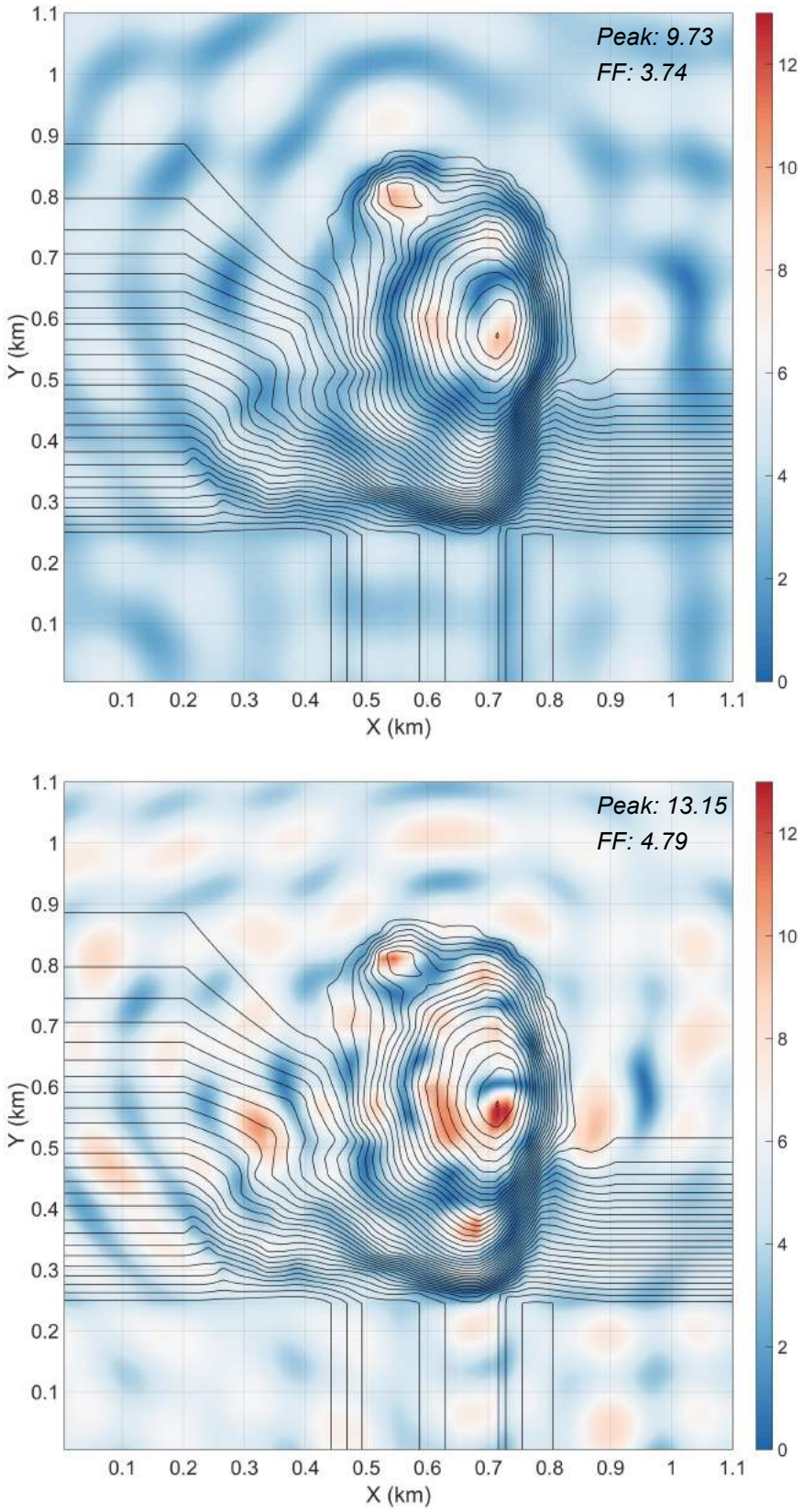

Figure 3.14. Transfer function amplitude of true layering, BK-KCC – ↑: $f = 13$ Hz, ↓: $f = 15$ Hz

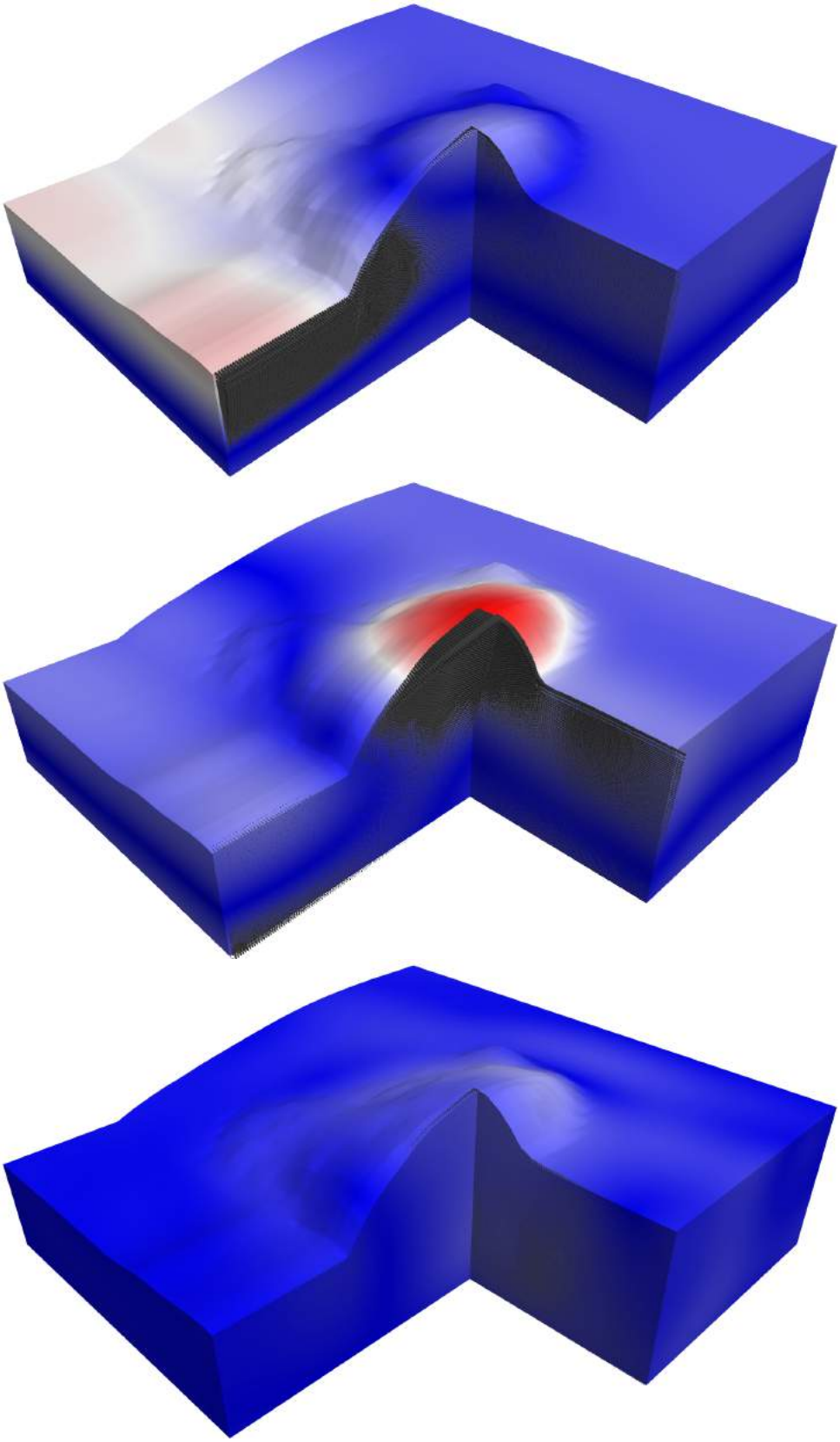

Figure 3.15. Snapshots of total wavefield, BK-KCC – (↑: 0.2s, ↔: 0.29s, ↓: 0.47s)

3.2 Strong Motion Station CI-LCP

The bird-eye view of CI-LCP site map is shown in Figure 3.16 along with its topographic map. The location of strong motion station is designated by a yellow triangle on the site map. Figure 3.17 shows the finite difference grids used for modeling wave propagation in homogeneous and layered cases. The material properties of different layers have been listed in Table 3.2 for each model. As compared to the site BK-KCC, which is characterized as a rock site, site CI-LCP has surface soft layers of considerable thicknesses. Therefore, we expect to see the coupling soil-topography effect more clearly. Furthermore, the geometry and material properties of near surface layers seems to be adequate for trapping the incoming wave. That is, having a different amplification pattern by adding soil layering to the homogeneous model is plausible. Another distinct feature of site CI-LCP is that it contains a set of topographic features (as compared to the isolated feature of site BK-KCC). Thereby, we can examine the combined effect of several adjacent features and see how it differs from the isolated case. Similar to the previous model, we applied two types of excitations at the base of each model: A single Ricker wavelet of central frequency f_0 = 3.5 Hz and an ensemble of three Ricker wavelets with central frequencies f_0 = 1, 3 and 7 Hz that are superposed at their center (Figures 3.3 and 3.4).

Polarization scenarios used for this site have been shown in Figure 3.18. Figures 3.19 to 3.21 show the amplification factor maps overlaid by topography contour lines of 5m interval respectively for homogeneous, V_{S30} and true layering cases. Since the feature is more symmetric with respect to the azimuth angle (compared to site BK-KCC), we see less difference between amplification factors/patterns of *X* and *Y* polarization scenario for homogeneous model. However, it is still evident that vertical/horizontal ridges are more amplified by *X*/*Y* polarized input motion (lines *A*, *B* and *C* vs. lines *D* and *E*). Larger amplification is observed at the intersection of horizontal and vertical ridges. Similar to the rock site, the pattern is consistent with the general topographic amplification i.e. amplification/de-amplification in convex/concave regions. Nevertheless, the presence of adjacent topographies and the consequent extra amplification and de-amplification regions alters the pattern to some extent. The amplification map of V_{S30} model (Figure 3.20) clearly shows how soil layering can change the amplification pattern.

While the free-field values are larger than the homogeneous case, the coupled values show less amplification in most regions (smaller factors over narrower regions). The general pattern of topographic amplification along convex and concave regions is no longer valid. The results get more surprising when we consider the true layering model. As we can see in Figure 3.21, the coupling effect renders a completely different amplification pattern: amplification now occurs along the canyons and de-amplification does so along the ridges. In addition, the top soft layers, which have an adequate thickness compared to the incident wavelength, play a decisive role in the overall amplification pattern. For the site CI-LCP, the V_{S30} model gives rise to lower amplification factors compared to the true layering case. Again, the amplification factors of layered models demonstrate the nonlinear coupling effect. For example, while the 1D site response of true layering shows 80% increase (1.80) with respect to the homogeneous case, the 3D amplification is only magnified 33% (2.98) for *Y* polarization and even less for *X*.

As in the case of rock site, we are able to observe the energy distribution among various frequency components the frequency response of topographic feature. Figure 3.22 shows the amplitude of 1D transfer function (surface to borehole) of site CI-LCP. It shows the fundamental frequency of the site i.e. f_0 = 21.4 Hz along with those frequencies of higher modes (located within the practical frequency range of interest).

Figures 3.23 to 3.27 show the amplitude of transfer function at various frequencies. Similar to the 1D case, the "3D transfer function" has several peaks and troughs over the frequency range of interest. Similar to the rock site, at lower frequencies, the large wavelength of incoming wave is barely seen by the feature and results in a coarser scattering pattern (Figures 3.23 and 3.24).

Increasing the frequency will result in finer scattering pattern as the incoming energy is captured by features of smaller size (Figure 3.26 and 3.27).

Figure 3.28 shows snapshots of the total wavefield at different time steps. The top plot depicts 1D site response over the lower part of the feature. The middle one corresponds to the moment of peak amplification along the ridges when we have maximum constructive interference between incoming shear and diffracted surface waves. The last plots shows that even after the direct wave reflected back to the medium, a considerable amount of energy remains in the upper layers which manifests as surface waves.

Figure 3.16. CI-LCP site – ↑: bird-eye view, ↓: topographic map

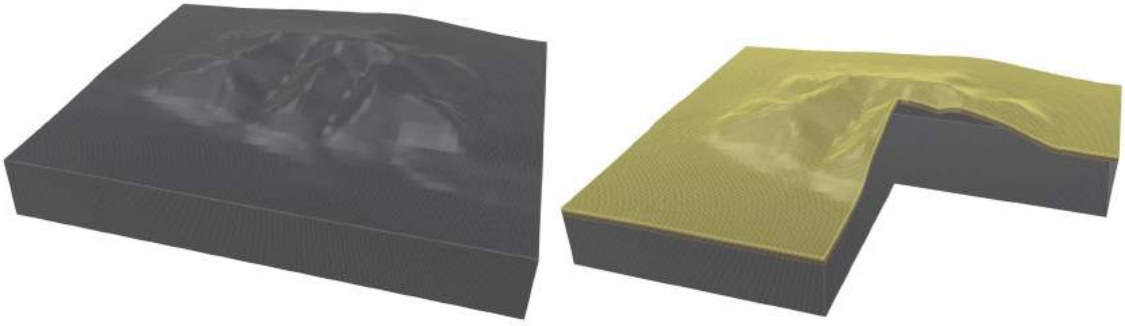

Figure 3.17. Numerical model used for CI-LCP station – ↑: homogeneous, ↓: true layered

Table 3.2. Thickness and material properties for different layering scenarios – site CI-LCP

Layering Scenario	Layer	Thickness (m)	V_S (m/s)	ν	ϱ (kg/m^3)
Homogeneous	1	---	486	0.333	2000
V_{S30}	1	30	267	0.333	1880
	2	---	486	0.333	2000
True Layering	1	7.0	179	0.333	1800
	2	17.0	255	0.333	1870
	3	---	486	0.333	2000

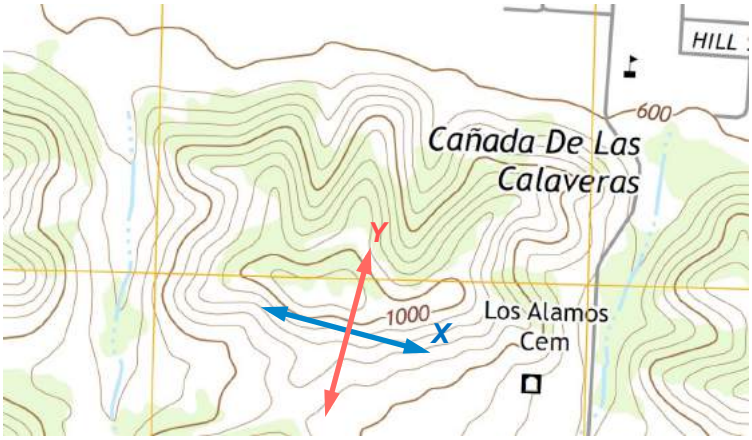

Figure 3.18. Polarization directions of input shear wave – site CI-LCP

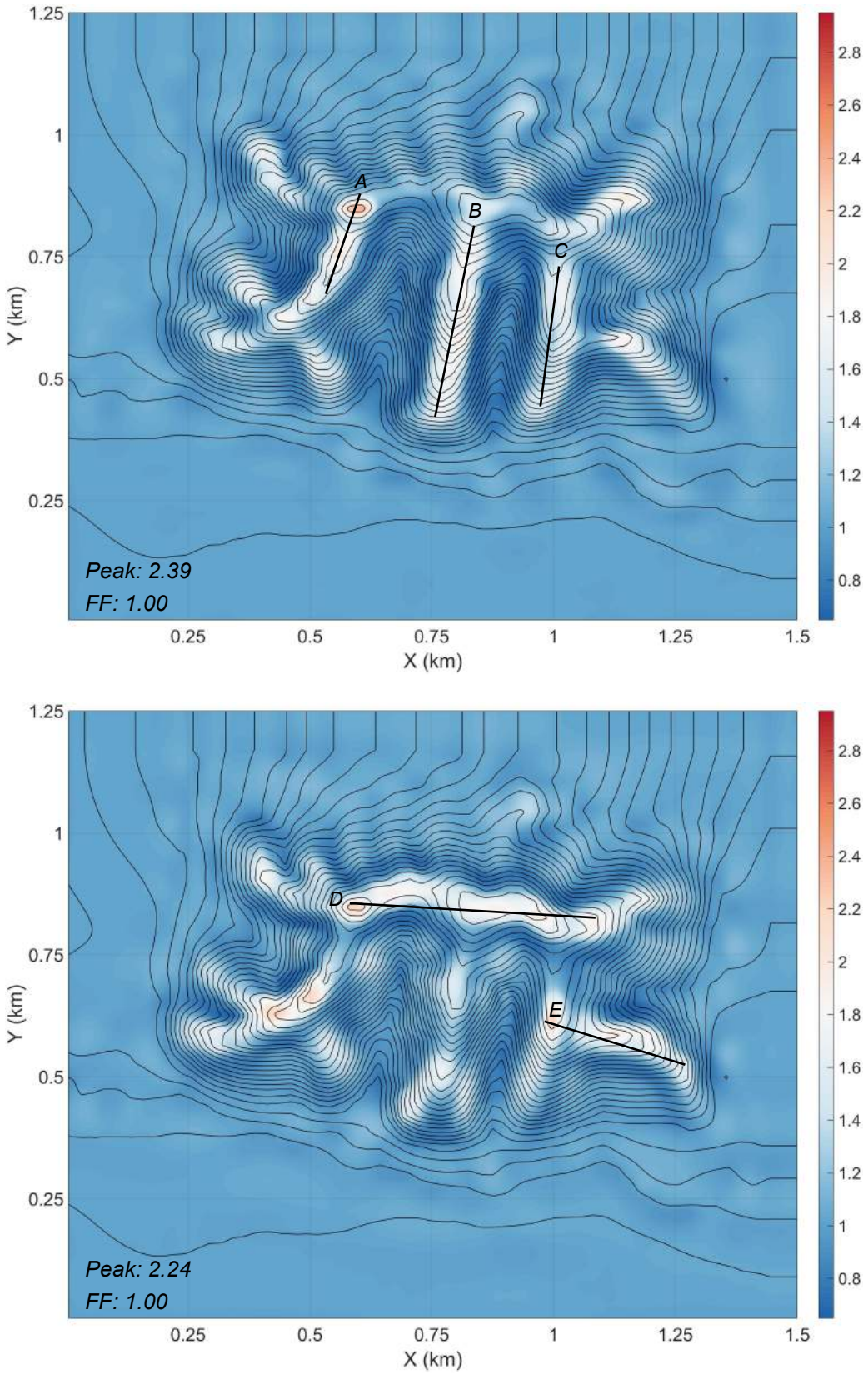

Figure 3.19. Amplification factor for homogeneous case, CI-LCP – ↑: X, ↓: Y polarization

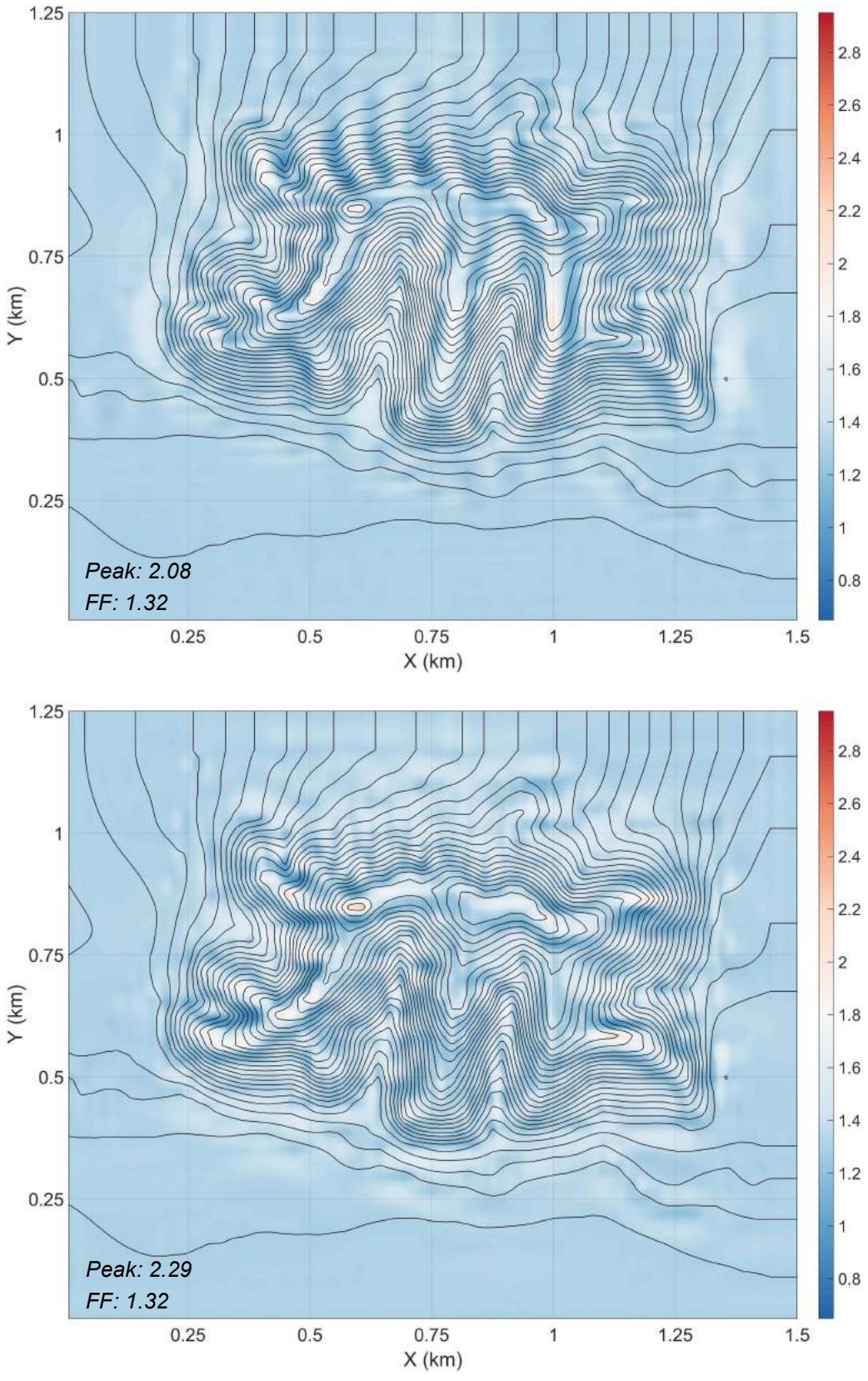

Figure 3.20. Amplification factor for V_{S30} case, CI-LCP – ↑: X, ↓: Y polarization

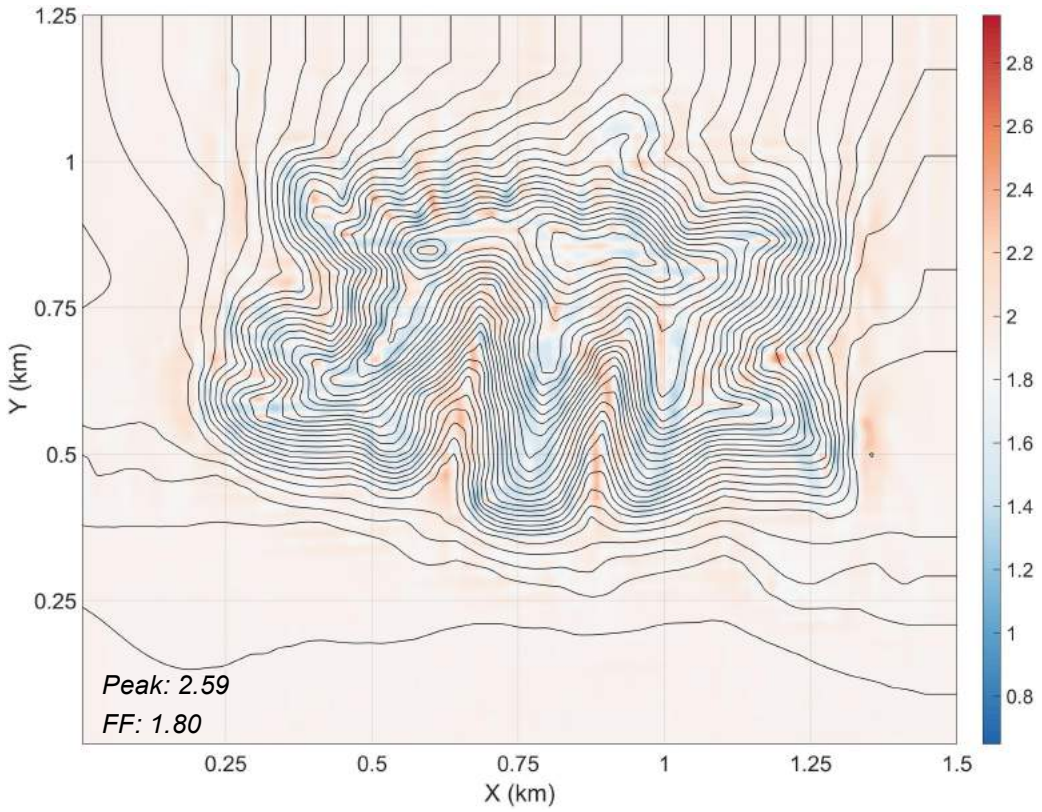

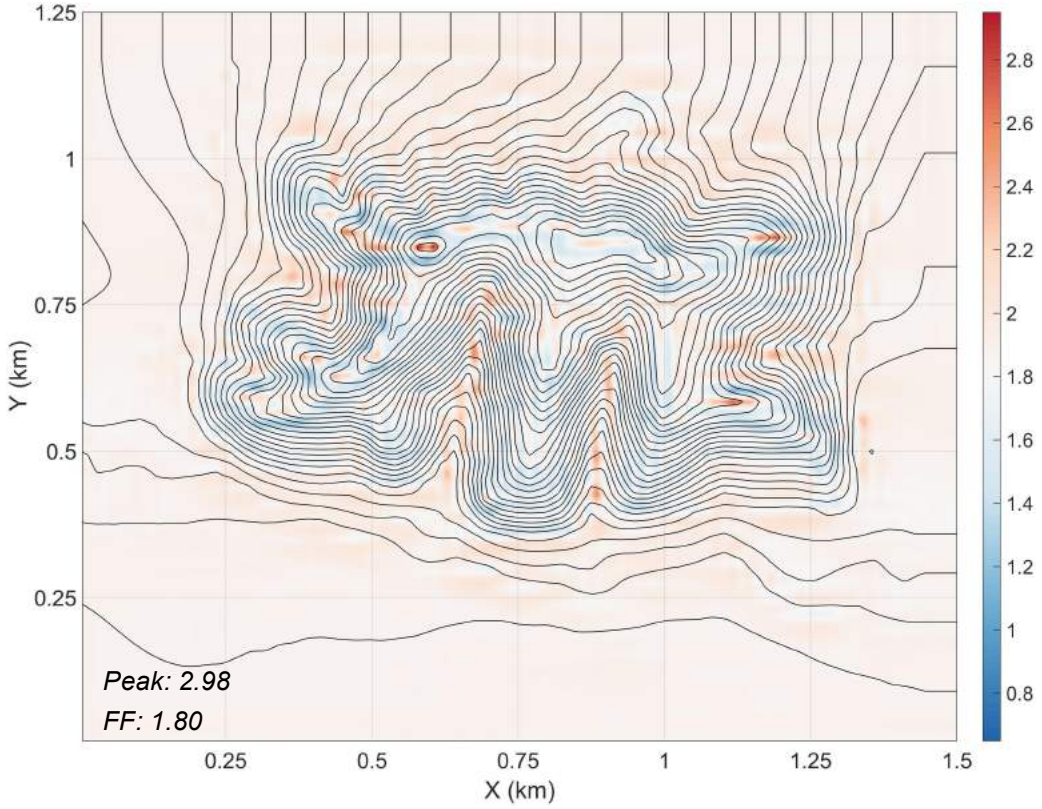

Figure 3.21. Amplification factor for true layering case, CI-LCP – ↑: X, ↓: Y polarization

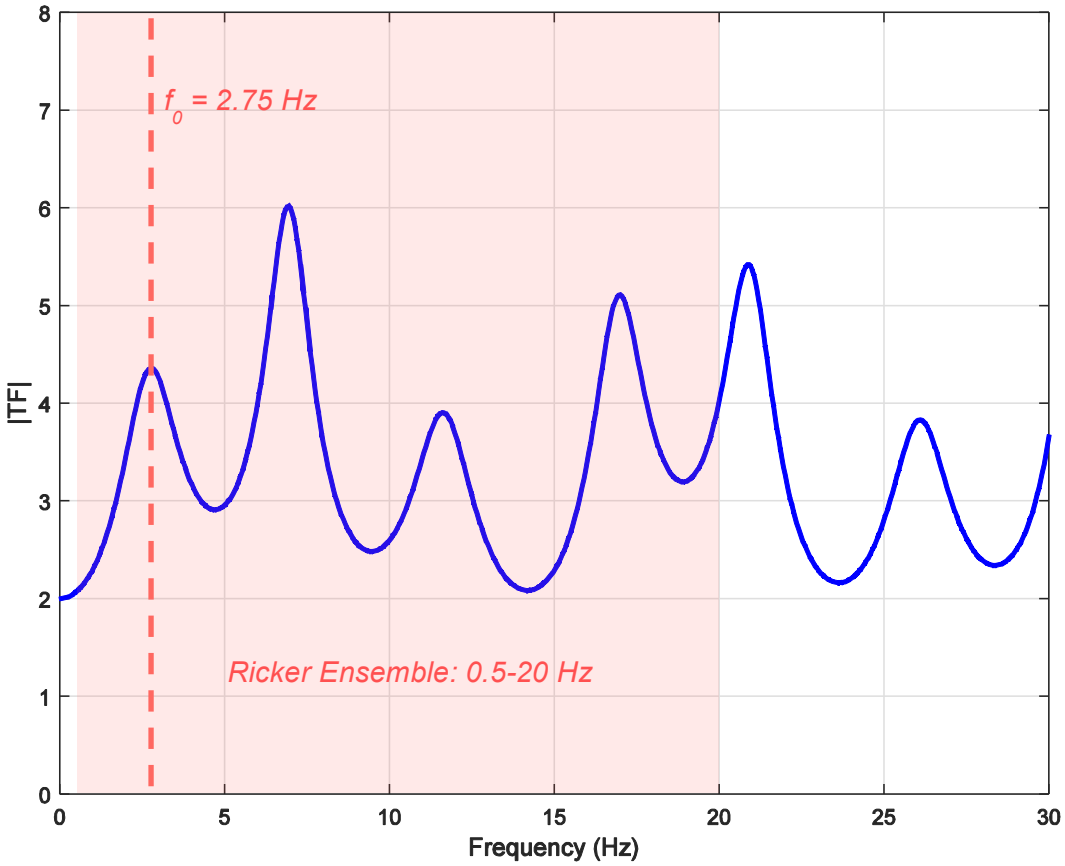

Figure 3.22. 1D transfer function for site CI-LCP

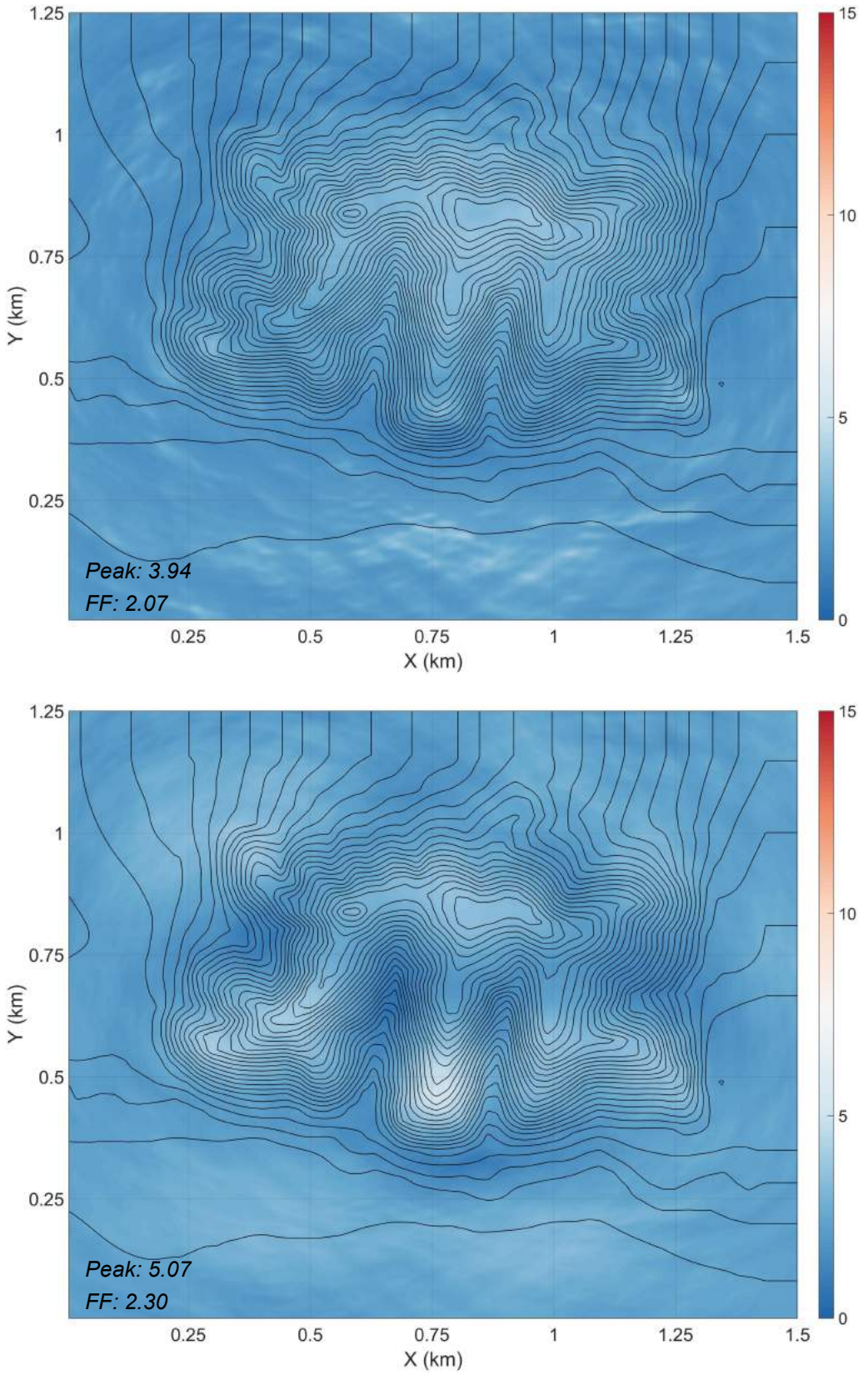

Figure 3.23. Transfer function amplitude of true layering, CI-LCP – ↑: $f = 0.5$ Hz, ↓: $f = 1$ Hz

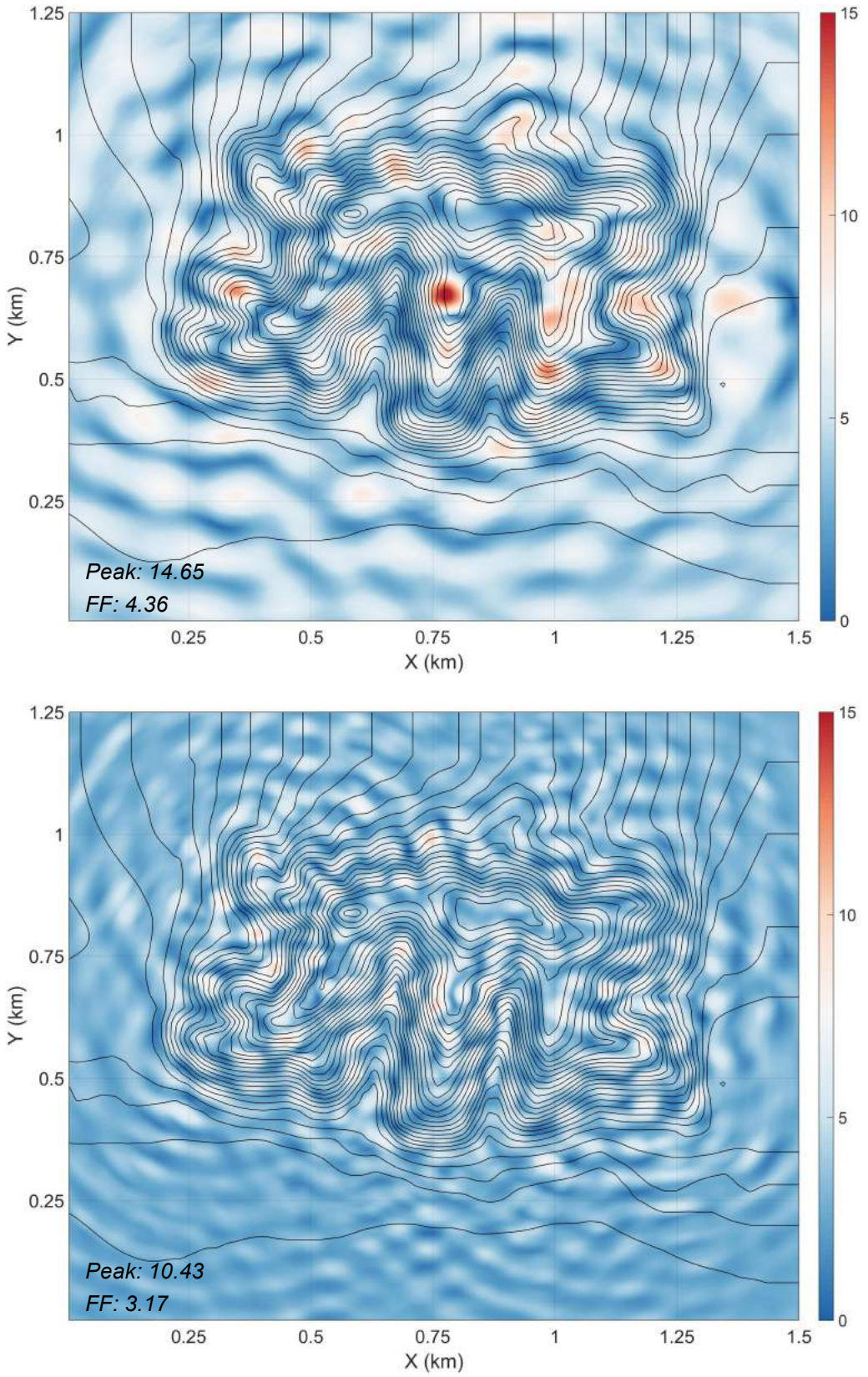

Figure 3.24. Transfer function amplitude of true layering, CI-LCP – ↑: $f = 2.75$ Hz, ↓: $f = 4$ Hz

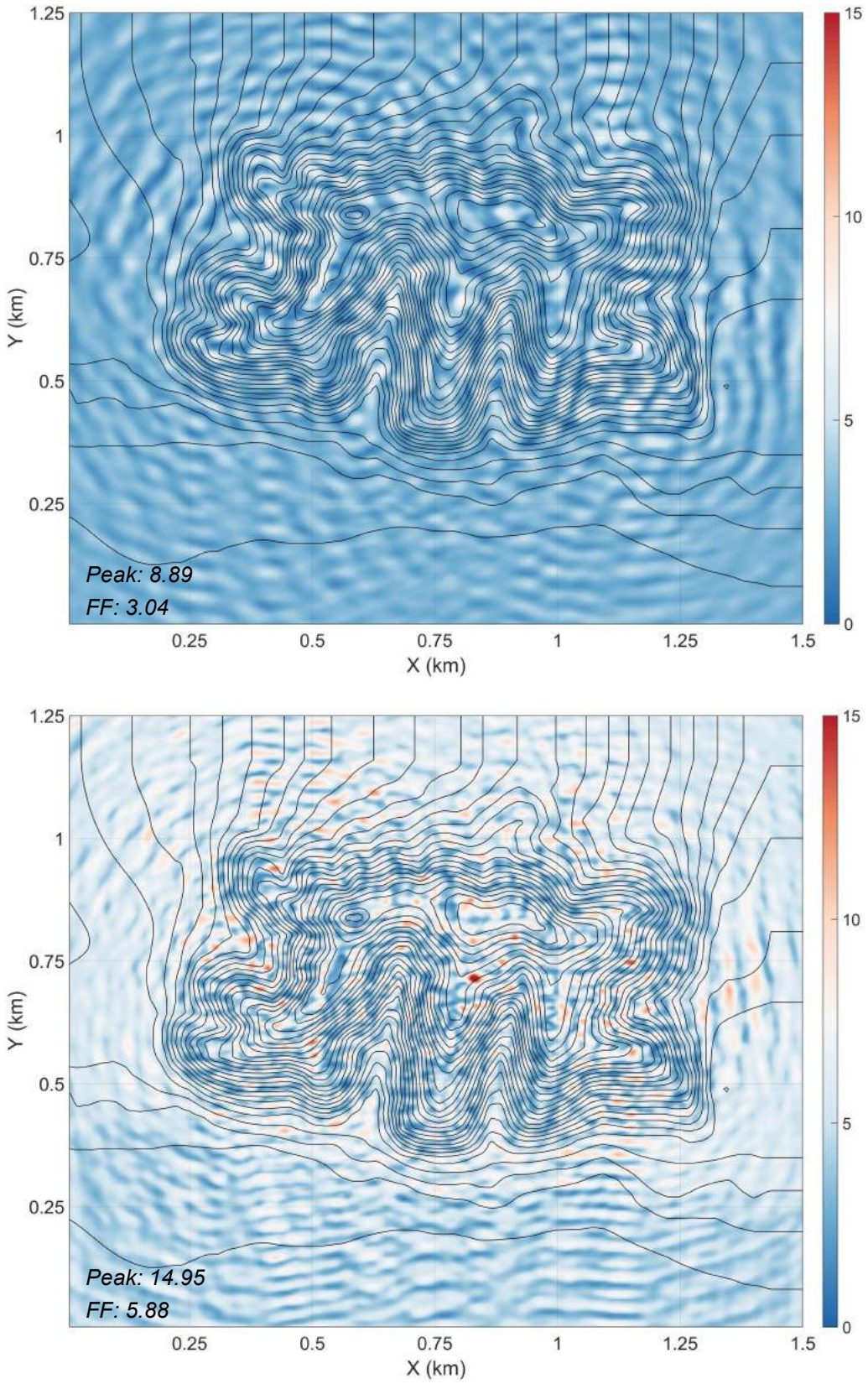

Figure 3.25. Transfer function amplitude of true layering, CI-LCP – ↑: $f = 5.2$ Hz, ↓: $f = 7.1$ Hz

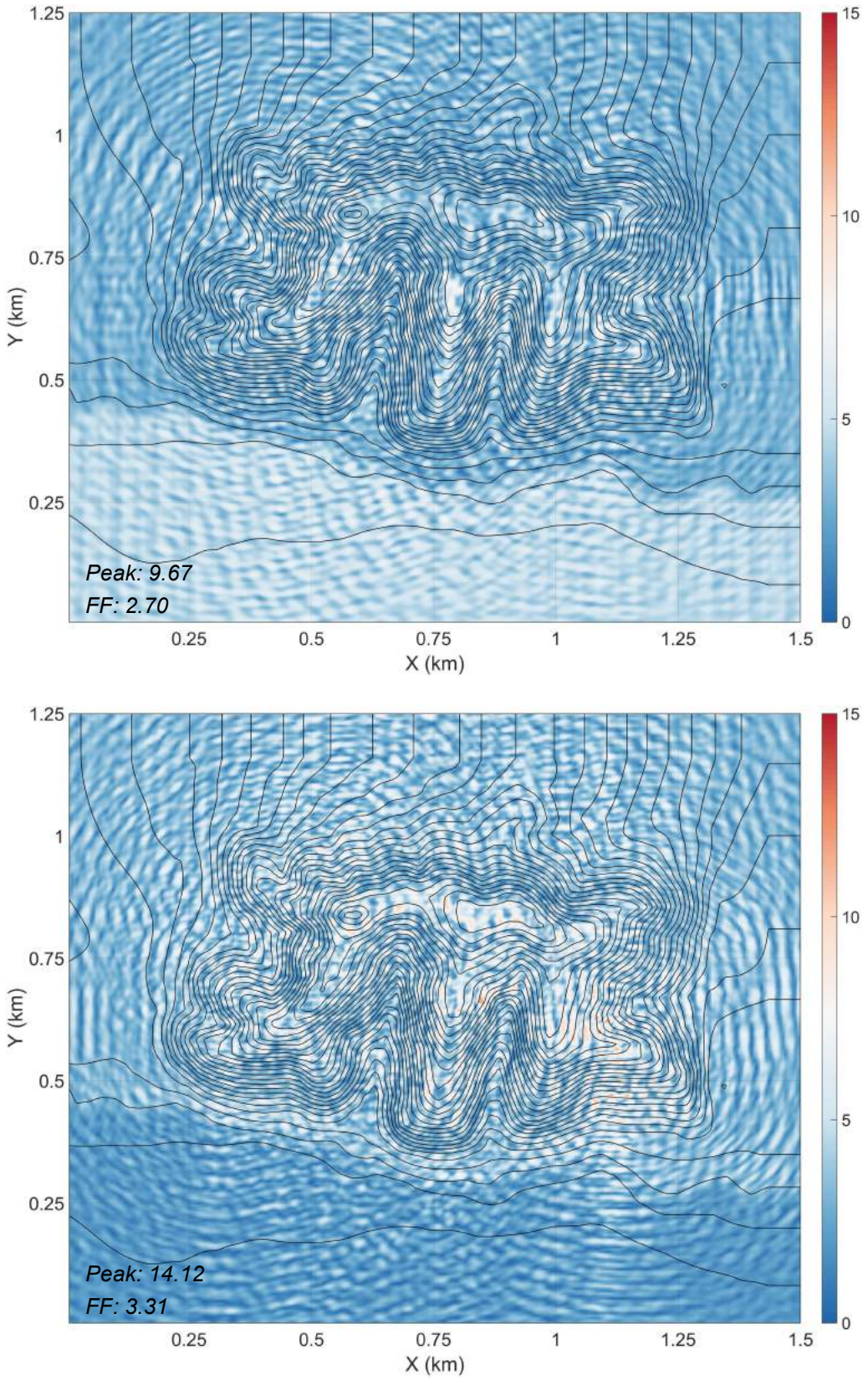

Figure 3.26. Transfer function amplitude of true layering, CI-LCP – ↑: $f = 10.2$ Hz, ↓: $f = 12.3$ Hz

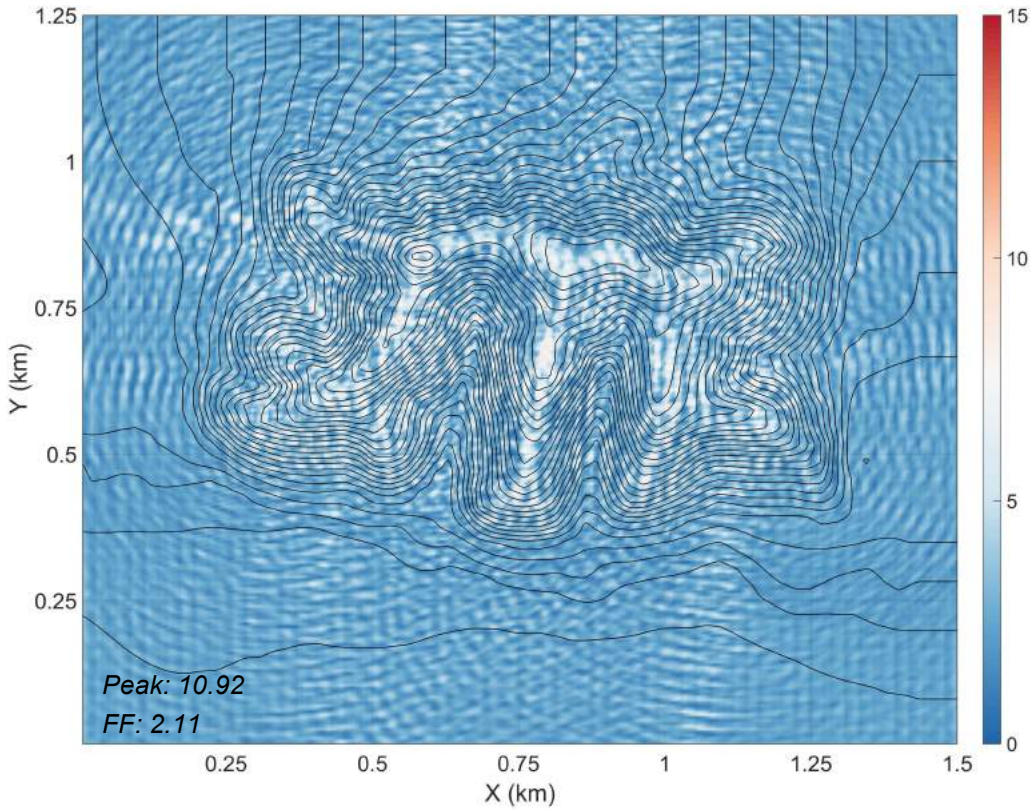

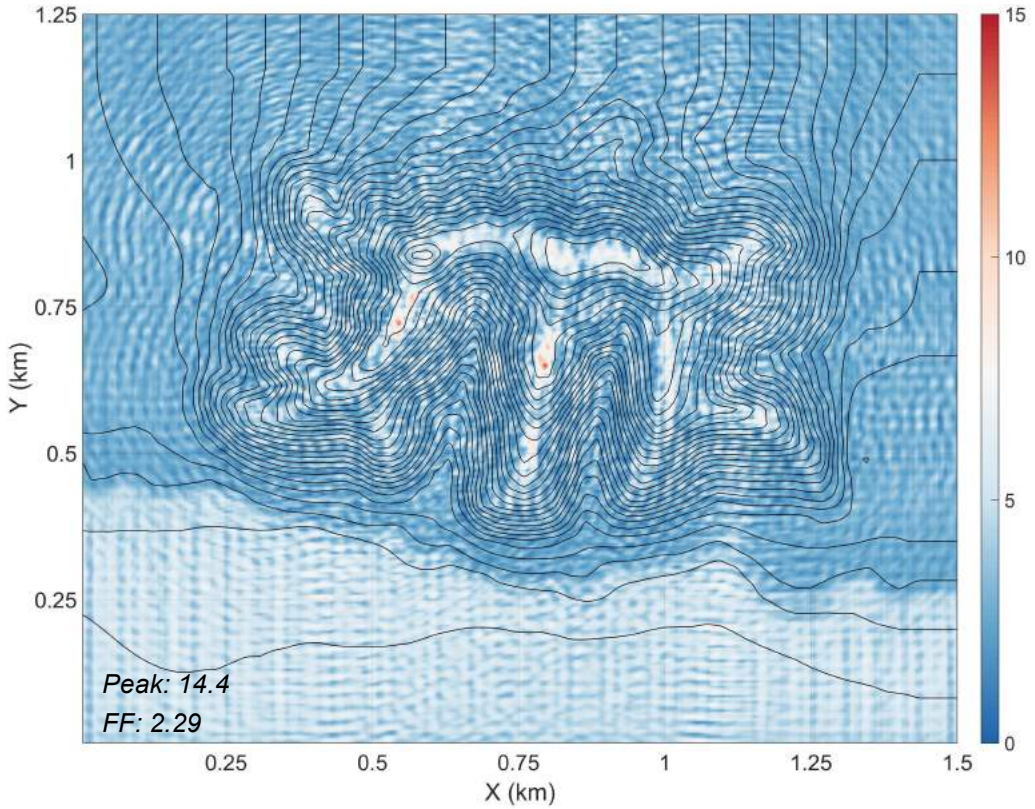

Figure 3.27. Transfer function amplitude of true layering, CI-LCP – ↑: $f = 13.9$ Hz, ↓: $f = 15$ Hz

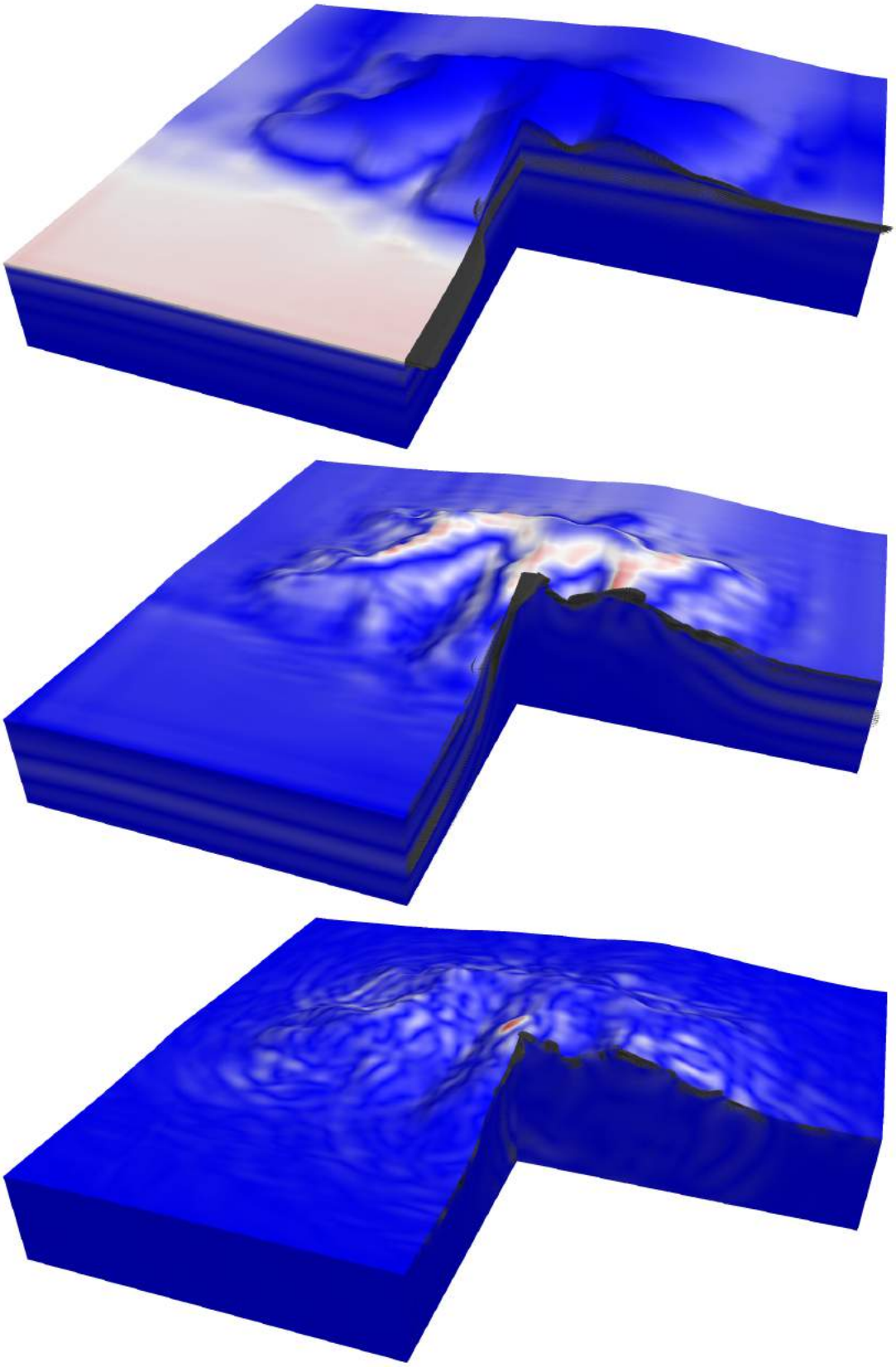

Figure 3.30. Snapshots of total wavefield, CI-LCP – (↑: 0.26s, ↔: 0.37s, ↓: 0.73s)

4. Conclusions

In this study, we investigated the coupling effects of surface topography and soil stratigraphy through a series of systematic analysis and case studies. We first built upon our previous work on the response of dam-type topographic features [4,24,25,42] and developed 2 types of idealized geometries. Controlling parameters of the latter in excess of those homogeneous dam-type geometry (see [1] for more information) include the thickness of upper layer and the stiffness contrast between two layers, normalized by the incident wavelength and by the far-field 1D site fundamental frequency and site amplification factors.

To keep the total number of possible cases within a practical range, we performed the analysis using fixed slope angle ($\alpha = 45°$) and dimensionless height ($\eta = 1$). For each layering scenario, amplification factors have been presented as a function of dimensionless width at several sets of dimensionless thickness and stiffness contrast. For the layered model with horizontal interface (*M1*), the scattered wavefield is similar to the homogeneous case as no scattering occurs at the interface. However, there exists a lower boundary at a finite depth bringing about multiple reflections. Since the amplitude of these reflections is not dominant (energy leakage at the interface), the form of amplification pattern is similar to that of homogenous case. Furthermore, the peak amplification factor of all parameter sets occurs at the same dimensionless width as in the homogeneous case ($\zeta = 0.88$). As for the effects of stiffness contrast and thickness, the former cluster the curves in distinct categories while the latter shows negligible impact.

The layered model of parallel interface (*M2*) contains several more sources of scattering and narrower surface region for trapping the incident energy compared to *M1*. Therefore, it involves a different wave mechanism and consequently a different amplification pattern (peaks and troughs are no longer coincide with homogeneous case). Furthermore, the thickness of upper layer has more influence on the form of amplification curves. It could be explained as the free surface boundary and interface act as a single scatterer whose characteristic length (thickness) controls the overall behavior. As for the single slope response, we observed that the threshold dimensionless width shifts toward larger values. The reflection of transmitted energy between two boundaries (free surface and interface) accounts for such oscillatory behavior. The spatial variation of amplification factors clearly shows the nonlinear coupling between soil and topography amplification, a pattern that is more dependent on the stratigraphy than the surface geometry of the feature. Finally, and to have a better understanding of soil-topography coupling effects in more realistic settings, two case studies have been presented and discussed. The results show that 3D layered model, which contains out-of-plane scattering effects in addition to 2D soil-topography effect, generally gives larger amplification factor. In addition, it can considerably change the amplification pattern compared to the homogeneous case. Finally, the V_{S30} model, which is very common in the seismic hazard studies, may overestimate or underestimate the overall response of topographic feature.

We then studied two case studies at strong motion stations located on irregular topographic features in California. We specifically combined digital elevation maps (DEM) and the ARRA USGS profiles [66] to develop finite volume models of irregular topography, stratigraphy and material properties. We considered 3 different layering scenarios: a homogeneous model, the same model but whose top 30m have been replaced by a 30 m homogeneous layer of velocity equal to VS30, and a model constructed using the site-specific profiles available at the station [66]. While the first model represents the pure topographic (geometric) amplification, the other two cases introduce soil-topography coupling effect at different levels of model complexity. Since VS30 is frequently the only data available on a regional scale that conveys information about the near surface soil stiffness, a simplified way to include topography-soil coupling effects could have potentially been to use VS30 as the velocity of a 30m soil layer. However, as we will demonstrate in the following sections, this approach may not only lead to erroneous results in

terms of amplification magnitude, but more importantly perhaps, in terms of spatial amplification pattern and frequency response. This lead to perhaps the most important conclusion of this study, namely that –contrary to their name-- topography effects are much less dependent on the ground surface topography than on the underlying stratigraphy, and that the same exact feature may yield completely different patterns and amplitudes of topographic amplification depending on the soil layering.

While not yielding a universal answer on how to predict this very complex, nonlinear problem, the significance of this project lies on the fact that numerous strong motion stations in the U.S. are located on topographic features; recent site characterization efforts [66] showed that several of these stations are installed on or in the vicinity of soft sediments. We thus hypothesized that ignoring 3D site effects may have so far been leading to biased ground motion predictions at sites located on elevated topography characterized by soft site conditions. We tested this hypothesis by developing canonical cases of idealized models of coupled soil-topography features, and detailed site-specific 3D models of selected station sites on irregular topography with underlying stiff and soft sediments, computing site-specific amplification factors that include the coupled effects of soil and topography, and assessing impact of the coupling effects relative to the simulated response of rock-outcrop ground motions (topography in absence of stratigraphy) as well as the response of rock-outcrop features whose top 30m were replaced by homogeneous 30 m deep layers of the V_{s30} velocity. At sites with strong impedance contrasts of soft surficial sediments to deeper stiff basement rock layers, the latter approximation failed to capture the coupling effects outside the wavelength range of 30m. The following sections describe our findings in detail, and highlight the needs for future research on the subject, particularly as it pertains to extreme ground motion predictions; parameterization of ground motion prediction equations; and physics-based simulated ground motions and hazard maps that properly parameterize and simulate 3D site effects in a way that integrates site, topography and coupling effects.

The most important finding of our work, therefore, is that the causative factor of what is frequently referred to as *topographic amplification* is not the ground surface geometry alone, but instead the nonlinear coupling of geometry and underlying soil stratigraphy that affects the amplitude, frequency, duration and direction of wave propagation, even if the underlying soil behavior is linear. Our findings have significant implications that we expect to see precipitating to extreme ground motion predictions; parameterization of ground motion prediction equations; and physics-based simulated ground motions and hazard maps, which should revisit, parameterize and simulate 3D site effects in a way that integrates site, topography and coupling effects thereof.

Publications and presentations on this project findings

1. Mohammadi, K. (2015). "Geometry and Stratigraphy Parameterization of Topography Effects: From the Infinite Wedge to 3D Convex Features" PhD thesis, Georgia Institute of Technology
2. Mohammadi K. and Asimaki D. (2016). "Three dimensional topography effects: Parametric investigation and site-specific analyses", Bulletin of the Seismological Society of America (in preparation)
3. Mohammadi K. and Asimaki D. (2016). "Soil-Topography coupling effect: Parametric investigation and site-specific analyses ", Bulletin of the Seismological Society of America (in preparation)
4. Mohammadi, K., & Asimaki, D. (2015). Topography effects: From infinite wedges to three-dimensional features. 6th International conference on earthquake geotechnical engineering, Christchurch, New Zealand
5. Mohammadi, K., & Asimaki, D. (2017). Topography Effects in ground motion are not topography effects after all. Geotechnical Frontiers, Orlando, FL

6. *Soil-Topography Coupling Effects at Strong Motion Stations in California*, Annual Meeting Seismological Society of America, Reno NV, 20-22 April, 2016
7. *Understanding, Parameterization and Simulations of 3D Topography Effects*, Annual Meeting Seismological Society of America, Pasadena CA, 21-23 April, 2015

Bibliography

1. Bouchon M. (1973). Effect of topography on surface motion, *Bulletin of the Seismological Society of America*, 63, 615-632.
2. Boore D.M (1972b). Note on the effect of topography on seismic SH waves, *Bulletin of the Seismological Society of America*, 62, 275-284.
3. Nagashima F., H. Kawase, S. Matsushima, F. J. Sanchez-Sesma, T. Hayakawa, T. Satoh, and M. Oshima (2012). Application of the H/V spectral ratios for earthquake ground motions and microtremors at K-NET sites in Tohoku region, Japan to delineate soil nonlinearity during the 2011 off the Pacific Coast of Tohoku earthquake, in Proceedings of the International Symposium on Engineering Lessons Learned from the 2011 Great East Japan Earthquake, Tokyo, Japan
4. Assimaki D., Gazetas G. and Kausel E. (2005a). Effects of local soil conditions on the topographic aggravation of seismic motion: Parametric investigation and recorded field evidence from the 1999 Athens Earthquake, Bulletin of the Seismological Society of America, 95(3)
5. Bard, P. Y. (1999). Local effects on strong ground motion: Physical basis and estimation methods in view of microzoning studies, *Proceedings, Advanced Study Course on Seismotectonic and Microzonation Techniques in Earthquake Engineering* 4, Kefallinia, Greece, pp. 127–218.
6. Geli L., Bard P.-Y. & Jullien B. (1988). The effect of topography on earthquake ground motion: a review and new results, *Bulletin of the Seismological Society of America*, Vol. 78, 42-63.
7. Faccioli E. (1991). Seismic amplification in the presence of geological and topographic irregularities, *Proceedings of the 2nd International Conference on Recent Advances in Geotechnical Earthquake Engineering and Soil Dynamics*, March 11-15, St Louis, Missouri, Vol. 2, 1779-1797.
8. Finn W.D.L. (1991). Geotechninal engineering aspects of seismic microzonation, *Proceedings of the 4th International Conference on Seismic Zonation*, August 25-29, Stanford, California, Vol. 1, 199-250.
9. Nechtschein S., Bard P.-Y., Gariel J.-C., Mèneroud J.-P., Dervin P., Cushing M., Gaubert B., Vidal S. & Duval A.M. (1995). A topographic effect study in the Nice region, *Proceedings of the 5th International Conference on Seismic Zonation*, October 17-19, Nice, France, 1067-1074.
10. Tucker, B., J. King, D. Hatzfeld, and I. Nersesov (1984), Observations of hard rock site effects, Bulletin of the Seismilogical Society of America, 74 (1), 121-136.
11. Bard P.-Y. (1982). Diffracted waves and displacement field over two-dimensional elevated topographies, *Geophys. J. R. Astr. Soc.*, Vol. 71, 731-760.
12. Boore, D.M. (1972a). Finite difference methods for seismic wave propagation in heterogeneous materials, In: B.A. Bolt (Editor), Methods in Computational Physics1, 1. Academic Press New York, NY, pp. 1-37.
13. Bouchon M. (1973). Effect of topography on surface motion, *Bulletin of the Seismological Society of America*, Vol. 63, 615-632.
14. Sánchez-Sesma F.J. & Campillo M. (1991). Diffraction of P, SV and Rayleigh waves by topographic features: a boundary integral formulation, *Bulletin of the Seismological Society of America*, Vol. 80, 2234-2253.

15. Sánchez-Sesma F.J. (1983). Diffraction of elastic waves by three-dimensional surface irregularities, *Bulletin of the Seismological Society of America*, Vol. 73, 1621-1636.
16. Sánchez-Sesma F.J. (1990). Elementary solutions for the response of a wedge-shaped medium to incident SH and SV waves, *Bulletin of the Seismological Society of America*, Vol. 80, 737-742.
17. Sánchez-Sesma, F. J. (1985). Diffraction of elastic SH waves by wedges, *Bull. Seismol. Soc. Am.* 75, 1435–1446.
18. Sánchez-Sesma, F. J., and E. Rosenblueth (1979). Ground motion at canyons of arbitrary shape under incident SH waves, Int. J. Earthquake Eng. Struct. Dyn. 7, 441–450.
19. Zhenpeng, L. Y., L. Baipo, and Y. Yifan (1980). Effect of three-dimensional topography on earthquake ground motion, Proceedings of the 7th World Conference on Earthquake Engineering, vol. 2, Istanbul, Turkey, September 8-13, 1980.
20. Bouchon, M., and Barker, J. S. (1996). Seismic response of a hill: The example of Tarzana, California, *Bull. Seismol. Soc. Am.* 86, 66–72.
21. Ashford S.A., Sitar N., Lysmer J. & Deng N. (1997). Topographic Effects on the Seismic Response of Steep Slopes, *Bulletin of the Seismological Society of America*, 87(3), 701-709
22. Ashford, S. A., and Sitar, N. (1997). Analysis of topographic amplification of inclined shear waves in a steep coastal bluff, Bull. Seismol. Soc. Am. 87, 692–700.
23. Bard, P. Y., and B. E. Tucker (1985). Ridge and tunnel effects: comparing observations with theory, Bull. Seism. Soc. Am. 75, 905–922.
24. Assimaki D., Kausel E. and Gazetas G. (2005b). Wave propagation and soil-structure interaction on a cliff crest during the 1999 Athens Earthquake, Soil Dynamics and Earthquake Engineering, 25(7-10), 513-527
25. Assimaki D., Kausel E. and Gazetas G. (2005c). Soil-dependent topographic effects: A case study from the 1999, Athens Earthquake, Earthquake Spectra, 21(4), 929-966
26. Olsen, K. B., and R. J. Archuleta (1996). Three-dimensional simulation of earthquakes on the Los Angeles fault system, Bull. Seismol. Soc. Am. 86, no. 3, 575–596.
27. Graves, R. W. (1998). 3-D finite-difference modeling of the San Andreas fault: source parameterization and ground motion levels, Bull. Seismol. Soc. Am. 88, 881–897.
28. Wald, D. J., and R. W. Graves (1998). The Los Angeles basin response in simulated and recorded ground motions, Bull. Seismol. Soc. Am. 88, 337–356.
29. Olsen, K. (2001). Three-dimensional ground motion simulations for large earthquakes on the San Andreas fault with dynamic and observational constraints, J. Comp. Acoust. 9, 1203–1214.
30. Pitarka, A., K. Irikura, T. Iwata, and H. Sekiguchi (1998). Three-dimensional simulation of the near-fault ground motion for the 1995 Hyogo-Ken Nanbu (Kobe), Japan, earthquake, Bull. Seismol. Soc. Am. 88, 428–440.
31. Furumura, T., and Hayakawa (2007). Anomalous propagation of long-period ground motions recorded in Tokyo during the 23 October 2004 Mw 6.6 Niigata-ken Chuetsu, Japan, earthquake, Bull. Seismol. Soc. Am. 97, 863–880.
32. Graves, R. W., and D. J. Wald (2004). Observed and simulated ground motions in the San Bernardino basin region for the Hector Mine, California, earthquake, Bull. Seismol. Soc. Am. 94, 131–146.
33. Benites, R., and K. B. Olsen (2005). Modeling strong ground motion in the Wellington metropolitan area, New Zealand, Bull. Seismol. Soc. Am. 95, 2180–2196.
34. Ewald, M., H. Igel, K. G. Hinzen, and F. Scherbaum (2006). Basin-related effects on ground motion for earthquake scenarios in the lower Rhine embayment, Geophys. J. Int. 166, 197–212.
35. Olsen, K., S. Day, J. Minster, Y. Cui, A. Chourasia, M. Faerman, R. Moore, P. Maechling, and T. Jordan (2006). Strong shaking in Los Angeles expected from southern San Andreas earthquake, Geophys. Res. Lett. 33, 575–596.

36. Wang, H., H. Igel, F. Gallovic, A. Cochard, and M. Ewald (2008). Sourcerelated variations of ground motions in 3-D media: application to the Newport–Inglewood fault, Los Angeles basin, Geophys. J. Int. 175, 202–214
37. Komatitsch, D., L. Qinya, J. Tromp, P. Suss, C. Stidham, and J. H. Shaw (2004). Simulations of ground motion in the Los Angeles basin based upon the spectral-element method, Bull. Seismol. Soc. Am. 94, 187–206.
38. Lee, S. J., H. W. Chen, Q. Liu, D. Komatitsch, B. S. Huang, and J. Tromp (2008). Three-dimensional simulations of seismic-wave propagation in the Taipei basin with realistic topography based upon the spectral element method, Bull. Seismol. Soc. Am. 98, 253–264.
39. Stupazzini, M., R. Paolucci, and H. Igel (2009). Near-Fault Earthquake Ground-Motion Simulation in the Grenoble Valley by a High-Performance Spectral Element Code, Bulletin of the Seismological Society of America, Vol. 99, No. 1, pp. 286–301.
40. Ma, S., R. J. Archuleta, and M. T. Page (2007), Effects of large-scale surface topography on ground motions, as demonstrated by a study of the San Gabriel Mountains, Los Angeles, California, Bulletin of the Seismological Society of America, 97, 2066-2079
41. Day, S. M., R. Graves, J. Bielak, D. Dreger, S. Larsen, K. B. Olsen, A. Pitarka, and L. Ramirez-Guzman (2008). Model for basin effects on long-period response spectra in southern California, Earthq. Specta, 24, 257–277.
42. Assimaki D.and Jeong S. (2013). Ground motion amplification observations at Hotel Montana during the M7.0 2010 Haiti Earthquake: Topography or soil amplification?, *Bulletin of the Seismological Society of America* (in print)
43. Graizer, V. (2009). Low-velocity zone and topography as a source of site amplification effect on Tarzana hill, California, *Soil Dynamics and Earthquake Engineering*, 29, 2, 324-332.
44. Yong, A., Martin, A., Stokoe, K., and Diehl, J., (2012), ARRA-funded Vs30 measurements at California and Central-eastern U.S. strong motion stations, U.S. Geol. Surv. Open-File Rept. (in review).
45. Francisco J. Chavez-Garcia, Luis R. Sanchez, and D. Hatzfeld (1996). Topographic Site Effects and HVSR. A Comparison Between Observations and Theory, Bulletin of the Seismological Society of America, Vol. 86, No. 5, pp. 1559-1573
46. Emeline Maufroy, Víctor M. Cruz-Atienza, and Stéphane Gaffeta (2012). A Robust Method for Assessing 3-D Topographic Site Effects: A Case Study at the LSBB Underground Laboratory, France, Earthquake Spectra, Volume 28, No. 3, pages 1–19
47. S. Lovati, M.K., H. Bakavoli, M.Massa, G.Ferretti, F. Pacor, R. Paolucci, E. Haghshenas and M. Kamalian (2011). Estimation of topographical effects at Narni ridge (Central Italy): comparisons between experimental results and numerical modeling, Bull Earthquake Eng 9:1987–2005
48. Roberto Paolucci, Ezio Faccioli & Fabio Maggio (1999). 3D Response analysis of an instrumented hill at Matsuzaki, Japan, by a spectral method, Journal of Seismology 3: 191–209
49. Annie Souriau, Agathe Roullé, and Christian Ponsolles (2007). Site Effects in the City of Lourdes, France, from H/V Measurements: Implications for Seismic-Risk Evaluation, Bulletin of the Seismological Society of America, Vol. 97, No. 6, pp. 2118–2136
50. Alan Yong, Antony Martin, Kenneth Stokoe, and John Diehl (2013). ARRA-funded V_{S30} measurements using multi-technique approach at California and central-eastern United States strong motion stations, Report OFR series No. 2013-1102
51. Martin A. and Stokoe K. (2013). EPRI (2004, 2006) Ground-Motion Model (GMM) Review Project: Shear Wave Velocity Measurements at Seismic Recording Stations, EPRI Report No. 3002000719 (http://www.epri.com/abstracts/Pages/ProductAbstract.aspx?ProductId=000000003002000719)

52. Ricardo Taborda and Jacobo Bielak (2013). Simulation and Validation of the 2008 Chino Hills, California, earthquake, Bulletin of the Seismological Society of America, Vol. 103, No. 1, pp. 131–156.
53. John G. Anderson (2004). Quantitative measure of the goodness-of-fit of synthetic seismograms, in Proc. 13th World Conf. on Earthquake Eng., Vancouver, British Columbia, Canada, Int. Assoc. Earthquake Eng., Paper 243.
54. Assimaki, Dominic, Wei Li, J. M. Steidl, and J. Schmedes (2008). Quantifying nonlinearity susceptibility via site response modeling uncertainty at three sites in the Los Angeles basin, Bulletin of the Seismological Society of America, 98(5), 2364-2390.
55. Li W. and Assimaki D. (2010). Site and ground motion dependent parametric uncertainty of nonlinear site response analyses in earthquake simulations, Bulletin of the Seismological Society of America, Vol. 100, No. 3
56. Assimaki D. and Li W. (2012). Site- and ground motion-dependent nonlinear effects in seismological model predictions, Soil Dynamics and Earthquake Engineering, Volume 32, Issue 1, January 2012, Pages 143-151
57. Peng, Z., C. Wu, and D. Assimaki (2012), Long-term change of site response and high-frequency radiations associated with the Mw9.0 Tohoku-Oki Earthquake in Japan, Seism. Res. Lett., 83, 278
58. Bonilla, L.F., Tsuda, K., Pulido, N., Regnier, J., and Laurendeau, A. (2011). "Nonlinear site resonse evidence of K-NET and KiK-net records from the 2011 Tohoku Earthquake." Earth Planets Space, 63, 1-7.
59. Assimaki D and Mohammadi K (2011). "Three-dimensional topographic amplification of seismic ground motion on an idealized convex feature", Annual Meeting Seismological Society of America, Memphis TN, April 11-13 2011
60. Aoi S, Obara K, Hori S, Kasahara K, Okada Y (2000) New Japanese uphole/downhole, strong-motion observation network: kiknet. Seismol Res Lett 72:239
61. Electric Power Research Institute (EPRI) (1993). Guidelines for determining design basis ground motions, Electric Power Research Institute Technical Report EPRI TR-102293.
62. Darendeli, M.B. (2001) "Development of a new family of normalized modulus reduction and material damping curves," Department of Civil, Architectural and Environmental Engineering. Austin, Texas: The University of Texas at Austin.
63. F. Panzera, G. Lombardo, and R. Rigano (2011). Evidence of Topographic Effects through the Analysis of Ambient Noise Measurements, Seismological Research Letters, v. 82, p. 413-419, doi: 10.1785/gssrl.82.3.413
64. Geoffrey P. Ely, Steven M. Day, and Jean-Bernard Minster (2010). Dynamic Rupture Models for the Southern San Andreas Fault, Bulletin of the Seismological Society of America, 100:131-150; doi:10.1785/0120090187
65. Li W. and Assimaki D. (2010). Simulating soil stiffness degradation in transient site response predictions, Soil Dynamics and Earthquake Engineering 30(5), pp. 299-309.
66. Yong, A., Martin, A., Stokoe, K., & Diehl, J. (2013). *ARRA-funded V S30 measurements using multi-technique approach at strong-motion stations in California and central-eastern United States* (No. 2013-1102). US Geological Survey.